Mag. Klemmer Olivia Anna-Katharina, BSc

Surface tension of the liquid iron-nickel system determined by means of electromagnetic levitation

MASTER'S THESIS

to achieve the university degree of

Diplom-Ingenieurin

Master's degree programme: Technical Physics

submitted to

Graz University of Technology

Supervisor

Ao.Univ.-Prof. Dipl.-Ing. Dr.techn. Gernot Pottlacher

Institute of Experimental Physics

Graz, June 2017

EIDESSTATTLICHE ERKLÄRUNG

AFFIDAVIT

Ich erkläre an Eides statt, dass ich die vorliegende Arbeit selbstständig verfasst, andere als die angegebenen Quellen/Hilfsmittel nicht benutzt, und die den benutzten Quellen wörtlich und inhaltlich entnommenen Stellen als solche kenntlich gemacht habe. Das in TUGRAZonline hochgeladene Textdokument ist mit der vorliegenden Masterarbeit/Diplomarbeit/Dissertation identisch.

I declare that I have authored this thesis independently, that I have not used other than the declared sources/resources, and that I have explicitly indicated all material which has been quoted either literally or by content from the sources used. The text document uploaded to TUGRAZonline is identical to the present master's thesis/diploma thesis/doctoral dissertation.

_____ _____

Datum / Date Unterschrift / Signature

Abstract

In this work, surface tension of the liquid iron-nickel system was measured by oscillating drop method using electromagnetic levitation. Experiments on liquid metals or alloys often face inherent contamination problems due to the high reactivity of this phase. The electromagnetic levitation setup of the thermo- and metalphyics group at Graz University of Technology provides a noncontact, containerless technique which overcomes these difficulties. The surface tension has already been determined for a large part of pure metals, in contrast, this thermodynamic property is widely unknown for alloys. This study tries to close some gaps, as the temperature dependence of surface tension was measured for two alloys, namely Fe-90% Ni-10% and Fe-60% Ni-40%, in addition to pure iron. These data are compared to reference data from literature if available, and to the so-called Butler model. Despite iron being in good conformity with the literature data and this theoretical concept, the experiments on the surface tension of the two alloys yielded different results than predicted by this model. Possible explanations for the discrepancy are developed and a concept for further implementations, which would then allow an elaborated investigation of possible causes of this alteration, is given at the end of this thesis. The additional experimental know-how and some results will be used for the work done in cooperation with the project partner Böhler, and consequently, enabling an improvement of numerical simulations of different melting processes.

Kurzfassung

In dieser Arbeit wurden die Oberflächenspannungen einiger Legierungen des Eisen-Nickel Systems basierend auf der Theorie des "Oscillating drop"-Technik mithilfe elektromagnetischer Levitation gemessen. Versuche an flüssigen Metallen werden durch Probleme mit Verunreinigungen, welche durch die erhöhte Reaktivität dieser Phase hervorgerufen werden, erschwert. Der elektromagnetische Versuchsaufbau der Thermo- und Metallphysik Gruppe der Technischen Universität Graz stellt eine kontaktlose, behältnisfreie Untersuchungsmethode dar und schafft es, diese Schwierigkeiten zu umgehen. Für einen Großteil der reinen Metalle wurde die Oberflächenspannung bereits bestimmt, im Gegenteil dazu ist diese für die meisten Legierungen noch unbekannt. Im Zuge dieser Arbeit wurde versucht, durch die Vermessung zweier Legierungen, nämlich, Fe-90% Ni-10% und Fe-60% Ni-40%, solche Lücken zu verkleinern. Darüber hinaus wurde auch reines Eisen untersucht. Im Anschluss wurden die erzielten Ergebnisse mit Literaturwerten, insofern vorhanden, und den theoretischen Berechnungen aus dem sogenannten Butler-Modell verglichen. Der Oberflächenspannungs-Temperatur Verlauf des reinen Eisens zeigte eine sehr gute Übereinstimmung mit anderen experimentellen Ergebnissen aus der Literatur und diesem Model. Abweichungen wurden hingegen für die Resultate der Legierungen festgestellt. Mögliche Erklärungen dieser Diskrepanz wurden diskutiert. Diese Arbeit schließt mit einem kurzen Ausblick auf eine zukünftige Erweiterung des Versuchsaufbaus und deren Vorteile. Diese würde eine genauere Untersuchung einer der denkbaren Ursachen dieser Abweichungen ermöglichen. Das im Zuge dieser Diplomarbeit erworbene experimentelle Wissen und einige Ergebnisse werden in der Arbeit mit dem Projektpartner Böhler genutzt und dienen einer verbesserten Simulation von unterschiedlichen Schmelzvorgängen.

Acknowledgment

It is a humbling experience to acknowledge those people who have helped me along the journey of my Master's thesis.

First of all, I would like to express my deepest sense of gratitude to the supervisor of my Master's thesis, Prof. Gernot Pottlacher, head of the thermophysics and metalphysics work group of the Institute of Experimental Physics at Graz University of Technology. I could not have imagined a better advisor for my thesis, as he consistently allowed me to follow my own ideas, while steering me in the right direction, whenever needed.
My sincere thanks to the Austrian Research Promotion Agency (FFG)[1] and our project partner Böhler for their support and the productive cooperation.
I especially want to thank Dipl. Ing. Thomas Leitner for introducing me to the field of electromagnetic levitation. Thank you for your unbelievable patience, understanding and for your insightful comments. It was a pleasure to work with you.
Furthermore, I am thankful to all other members of the work group: Dipl. Ing. Matthias Leitner and Dip. Ing. Peter Pichler for their positive and constructive attitude and for creating such an enjoyable atmosphere. I want to express my gratitude to the whole Institute of Experimental Physics for creating such a productive environment and its head Prof. Wolfgang Ernst for the opportunity to join the Institute for my Master Thesis.
Thank you Manuel for your selfless, patient support, your outstanding scientific know-how and your never ending trust in my talents.
Finally, I would like to thank my mum and my sister, the strongest and most inspiring women I know, for the unlimited encouragement and love they have provided me over the years.

[1] FFG project 855678: 'Surfacetension-Steel'

This work is dedicated to my dad. You are deeply missed.

Contents

CHAPTER 1

Motivation

For a vast majority of all industrially formed metal parts the production starts with the liquid metal/alloy. Computer-based simulations allow modelling of casting, melting and remelting processes, heat transport, predictions of microstructures and many other processes. A key limitation to the successful introduction of these models is the lack of precise thermophysical properties, such as surface tension, density, viscosity, enthalpy, specific heat capacity, thermal conductivity and specific electrical resistance.

In this thesis, surface tension and density as a function of temperature of liquid Iron-Nickel alloys will be studied by means of the levitating drop method. Investigations of metals and alloys in the liquid phase often face contamination problems due to the high reactivity caused by the high temperature. Owing to this difficulty, a non-contact, container-less technique would bypass this challenge. Thus, the electromagnetic levitation (EML) setup of the thermophysics and metalphysics group at Graz University of Technology (TU Graz) provides an elegant and superior method to measure surface tension and density of highly reactive melts at high temperatures. The resulting data sets will be used by our project[2] partner Böhler to improve the numerical models of the following two processes, namely Vacuum Arc Remelting and Gas-Atomizing for which surface tension and density pose important input parameters. These insights provide the basis for advancements in simulation and for a further optimization of the fabrication cycles and consequently their economic efficiency.

[2] FFG project 855678: 'Surfacetension-Steel'

CHAPTER 2

Introduction

When measuring thermophysical data of liquid metals, one has to overcome the problem of sample's contamination due to chemical reactions with the environment, especially the sample holder. This can either be done by using subsecond techniques to reduce the reaction time, e.g. ohmic pulse-heating, or by using container-less methods, like electromagnetic levitation, to hover the sample[3]. Both designs are used by the thermophysics and metalphysics work group at Graz University of Technology.

In comparison to the exploding wire technique, electromagnetic levitation allows the creation of a steady state of the liquid sample over a relatively long time regime. Also investigations of thermophysical properties of a sample in a metastable phase, like surface tension or density in the undercooled phase, become possible due to the strong inhibition of contamination [1].

This section aims to give a short introduction to the physical background of electromagnetic levitation and the theory of the oscillating drop technique, a noncontact method used to evaluate the specimen's surface tension. Furthermore, the main components of the experimental setup will be explained. The container-less positioning of the sample by means of levitation along with a noncontact measurement technique for surface tension determination is a powerful setup especially for the investigation of highly reactive metals. For more detailed information, the according literature sources are referred. The present experimental setup has been built by Aziz [2] and Schmon [3] and is presented in a wider range in their PhD thesis. Further improvements have been done by Leitner [4].

[3] other set-ups use electrostatic, aerodynamic or acoustic methods

2.1 Specimen levitation by electromagnetic force

Electromagnetic levitation is the most common technique for experiments involving levitation of liquid metals [5]. One of the levitation device's main component is a conically formed coil which creates an inhomogeneous electromagnetic field between the top and bottom part of the coil (see figure 2.1). The water-cooled coil is supplied by an alternating current with a radio frequency of approximately 380 kHz. If a conducting, diamagnetic sample is inserted into the magnetic field, the following two effects can be seen:

- **Inductive heating of the sample:**
  Eddy currents are induced inside the metallic material by the surrounding field with angular velocity of the field ω. This leads to a heating of the sample due to ohmic losses. Additionally, the currents evoke material flows leading to a constant material mixing, which consequently prevents segregation. The time-averaged absorbed power (heating power) P, which is proportional to the squared magnetic induction B, can be approximated by

$$P = -\frac{3\pi R_s}{\sigma \mu_0^2} H\left(\frac{R_s}{\delta}\right) B^2 \propto B^2 \ , \tag{2.1}$$

  with R_s the radius of the sample, σ the electrical conductivity of the sample, μ_0 the magnetic permeability, and H a function of the relation of the sample radius to δ, its skin depth, which is given by

$$\delta = \sqrt{\frac{2}{\omega \sigma \mu_0}} \ . \tag{2.2}$$

- **Positioning of the sample:**
  To levitate a specimen, the downward directed gravitational force needs to be compensated. The interaction of the induced eddy currents with the external electromagnetic field of the coils creates a lifting Lorentz force, pushing the sample into regions of lower field strength, and ultimately balancing gravity. Thus the specimen gets caged in this region, which is also illustrated in figure 2.1. The time-averaged force acting

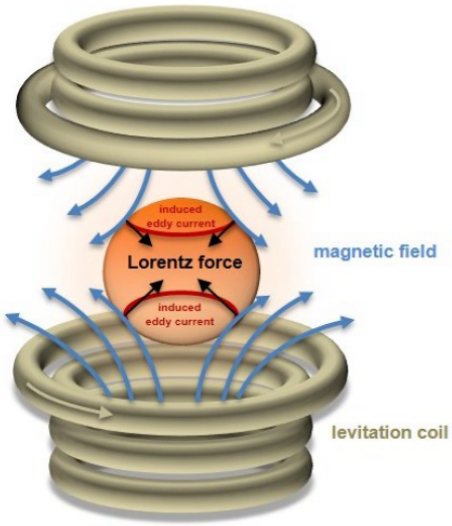

Figure 2.1: Illustration of electromagentic levitation principle, showing the levitation coil, the magnetic field lines, the induced eddy currents and the direction of the Lorentz force. The magnetic field of the levitating coil results in an opposing magnetic field of the sample, and hence a positioning and heating of the specimen. Source of image: [3].

on a spherical sample is proportional to the gradient of the magnetic induction B

$$\vec{F} = -\frac{\pi R_s^3}{\mu_0} G\left(\frac{R_s}{\delta}\right) \nabla B^2 \propto -\nabla B^2 \ . \tag{2.3}$$

The function of the relation of R_s to δ is denoted with G. The mathematical theory can be found in [1].

Gravitational and electromagnetic forces are acting on the sample, also leading to a deformation of its shape, generating characteristic surface oscillations. Being the restoring force, the liquid droplet's surface tension can thus be determined. The method which links these periodic deformations to the surface tension is called oscillating drop method and is presented in the following section 2.1.1.

2.1.1 Theory of the oscillating drop method

In the former section, the container-less method of electromagnetic levitation has been explained. To sustain the advantages of totally minimized sample-environment reactions, non-contact measuring methods have to be used. The oscillating drop method is based

on Rayleigh's theory which relates the sample's surface oscillation modes to its surface tension. These periodic surface changes are recorded by an imaging system which ensures non-contact measuring. The technical information about the image acquisition system can be found in section 3.1.

When the conducting sample gets electromagnetically levitated and heated up from the solid to the liquid phase, the specimen forms a sphere to minimize free surface energy. Periodic deformations around its spherical equilibrium shape can be observed. These capillary waves are restricted by the surface tension acting as restoring force and holding the specimen together. The changes in the droplet's radius δR as a function of polar angle ϑ, azimuthal angle ϕ, and time t can be described mathematically by the sum of spherical harmonics Y_l^m [6],

$$\delta R_s(\vartheta, \phi, t) = \sum_{l \geq 0} \sum_{m=-l}^{m=+l} a_{l,m}(t) \cdot Y_l^m(\vartheta, \phi) \ , \tag{2.4}$$

with $a_{l,m}(t)$ the time dependent amplitude of deformation, l the degree and m the order of the spherical harmonic function. The specimen's shape is approximated by the superposition of all oscillation modes.

For $l = 0$, the oscillation mode describes changes in the sample's radius. Assuming incompressible fluids, this mode is not allowed. The mode $l = 1$ corresponds to a translation of the specimen's center of mass without surface distortion [7]. Only oscillations with the condition $l = 2$ will be considered. The corresponding geometries are illustrated in figure 2.2. Oscillations with a mode $l > 2$ show too small amplitudes and are neglected for this reason [2].

In 1879 Lord Rayleigh [8] related the surface tension γ of a non-rotating, unconstrained specimen of spherical geometry and mass M to its surface oscillation frequencies ω

$$\omega_l^2 = l(l-1)(l+2) \cdot \frac{4}{3} \cdot \frac{\pi\gamma}{M} \ . \tag{2.5}$$

Note that ω_l^2 in formula 2.5 does not depend on the index m. Correspondingly, this frequency is $(2l+1)$-fold degenerated.

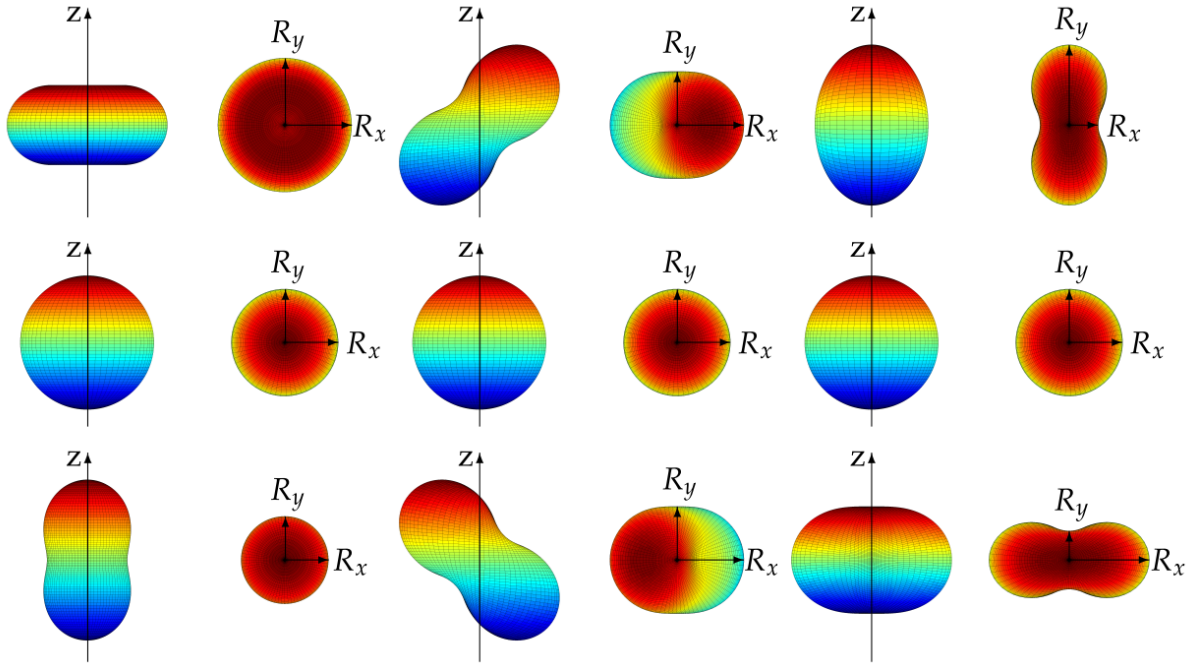

(a) $|m| = 0$ (b) $|m| = 1$ (c) $|m| = 2$

Figure 2.2: Visualization of oscillation modes $l = 2$ for (a) $m = 0$, (b) $|m| = 1$, (c) $|m| = 2$ with side view in the left column and top view in the right column. From top to bottom, maximum negative amplitude, zero amplitude and maximum positive amplitude are illustrated. R_x and R_y denote two arbitrary perpendicular radii. The z-axis is parallel to the gravtiy axis. Source of image: [2].

The most pronounced oscillation mode is of the degree $l = 2$ and is called Rayleigh frequency ω_R or fundamental frequency. Equationv2.5 yields for the Rayleigh frequency

$$\gamma = \frac{3}{32} \cdot \pi M \omega_R^2 = \frac{3}{8} \cdot \pi^3 M \nu_R^2 \ , \tag{2.6}$$

with $\omega = 2\pi\nu$. The fundamental frequency can split up into a maximum of five vibration bands.

Formula 2.5 only applies in case of extraterrestrial (non-gravity) or microgravity experiments. Under terrestrial conditions, gravitional and electromagnetic levitation forces are acting on the liquid specimen in opposite direction, but of equal size. When integrating over the whole droplet's volume, these forces cancel each other out. This doesn't hold true for the surface. The remaining residual forces lead to distortions forming an aspherically shaped droplet [5]. Supposing rotational symmetry along the z-axis of the droplet, which is set parallel to the gravity axis, results in case of $l = 2$ into three unequally spaced frequencies, correspond to $m = 0$, $m = \pm 1$ and $m = \pm 2$. These mode types are visualized in figure 2.2. In case of a linear magnetic field (proof of the approximation of the magnetic levitation field by a linear field can be found in [9]) the frequencies are altered by the mean square translation frequency $\overline{\omega_t^2}$ [7]

$$\omega_{2,0}^2 = \omega_R^2 + \overline{\omega_t^2} \left(3.832 - 0.1714 \cdot \left(\frac{z_0}{r}\right)\right)^2 \ , \tag{2.7}$$

$$\omega_{2,|\pm 1|}^2 = \omega_R^2 + \overline{\omega_t^2} \left(3.775 + 0.5143 \cdot \left(\frac{z_0}{r}\right)\right)^2 \ , \tag{2.8}$$

$$\omega_{2,|\pm 2|}^2 = \omega_R^2 + \overline{\omega_t^2} \left(-0.9297 + 2571 \cdot \left(\frac{z_0}{r}\right)\right)^2 \ , \tag{2.9}$$

$$\overline{\omega_t^2} = \frac{1}{3} \cdot \sum_{j=1}^{3} \omega_{t,j}^2 \ , \tag{2.10}$$

$$r = \sqrt[3]{\frac{3}{4} \cdot \frac{M}{\pi\rho}} \ , \tag{2.11}$$

where r is the radius of a sample of density ρ. The translation frequency in j-direction is represented through $\omega_{t,j}$. Cummings and Blackburn [7] proofed that in case of a linear intensity change of the magnetic field along the z-axis, the angular frequency $\omega_{t,z}$ of the vertical motion is supposed to have the a value equal to the sum of $\omega_{t,x}$ and $\omega_{t,y}$, the

translation frequency in the xy-plane:

$$\omega_{t,z} = \omega_{t,x} + \omega_{t,y} \ . \tag{2.12}$$

The factor z_0 denotes

$$z_0 = \frac{g}{2 \cdot \overline{\omega_t^2}} \ , \tag{2.13}$$

with g the gravitational acceleration. Adding up the angular frequencies $\omega_{2,0}^2$, $2\omega_{2,|\pm1|}^2$ and $2\omega_{2,|\pm2|}^2$ leads to the following sum-formula for the Rayleigh frequency [7]

$$\omega_R^2 = \frac{1}{5} \cdot (\omega_{2,0}^2 + 2 \cdot \omega_{2,|\pm1|}^2 + 2 \cdot \omega_{2,|\pm2|}^2) - \overline{\omega_t^2} \left(1.90 + 1.20 \cdot \left(\frac{z_0}{R}\right)\right)^2 . \tag{2.14}$$

If the assumption of non-rotation can't be presumed, then the modes with $m \neq 0$ split up proportional to the rotational frequency Ω into [10]

$$\omega(\Omega)_{l,m} = \omega_{l,|m|}(0) + \frac{m}{l} \cdot \Omega \ . \tag{2.15}$$

The split of mode with $|m| = 2$ is therefore expected to be twice as large as for $|m| = 1$. This criterium is used to facilitate the mode assignment of the peaks (see section 2.1.2). Under terrestrial conditions with droplet-rotation the m-degeneracy is completely removed and the spectrum of the fundamental mode should show five distinguishable peaks for $m \in \{-2, -1, 0, +1, +2\}$.

If the observed angular frequencies can be clearly attributed to the different modes (an assignment method is presented in section 2.1.2), then formula 2.14 can be used with

$$\omega_{l,|\pm m|} = \frac{1}{2} \cdot (\omega_{l,+m}(\Omega) + \omega_{l,-m}(\Omega)) \tag{2.16}$$

due to the symmetrical splitting. If a distinct assignment is not possible, equation

$$\omega_R^2 = \frac{1}{5} \cdot \left(\sum_{m=-2}^{m=+2} \omega_{2,m}^2 \right) - \overline{\omega_t^2} \left(1.90 + 1.20 \cdot \left(\frac{z_0}{R} \right) \right)^2 \tag{2.17}$$

is used alternatively.

Therefore, the surface tension can be evaluated with the help of equations (2.6), (2.14) and (2.17) by

$$\gamma = \frac{3}{8} \cdot \pi M \left\{ \frac{1}{5} \cdot \left(\nu_{2,0}^2 + 2 \cdot \nu_{2,|\pm 1|}^2 + 2 \cdot \nu_{2,|\pm 2|}^2 \right) - \overline{\nu_t^2} \left(1.90 + 1.20 \cdot \left(\frac{z_0}{R} \right) \right)^2 \right\}, \tag{2.18}$$

$$\gamma = \frac{3}{8} \cdot \pi M \left\{ \frac{1}{5} \cdot \left(\sum_{m=-2}^{m=+2} \nu_{2,m}^2 \right) - \overline{\nu_t^2} \left(1.90 + 1.20 \cdot \left(\frac{z_0}{R} \right) \right)^2 \right\}. \tag{2.19}$$

Because of the use of frequencies instead of angular frequencies in the equations (2.18) and (2.19), these equations turn into

$$\overline{\nu_t^2} = \frac{\overline{\omega_t^2}}{(2\pi)^2} = \frac{1}{3} \cdot \sum_{j=1}^{3} \nu_{t,j}^2 \ , \tag{2.20}$$

$$z_0 = \frac{g}{2 \cdot (2\pi)^2 \cdot \overline{\nu_t^2}} \ , \tag{2.21}$$

whereas R remains unchanged.

2.1.2 Method of mode assignment for the fundamental frequency

A fast Fourier Transform (FFT) algorithm computes the spectra of the surface oscillation frequencies and the sample translation frequencies. Thus, periodic changes in radii and the movements of the specimen's center of mass in the horizontal plane are converted to representative peaks in the frequency domain. To allow a distinct peak identification a method of mode assignment has been developed. Therefore the sum R_+ and the difference R_- of two arbitrary perpendicular radii are formed

$$R_+ = R_x + R_y \ , \tag{2.22}$$

$$R_- = R_x - R_y \ . \tag{2.23}$$

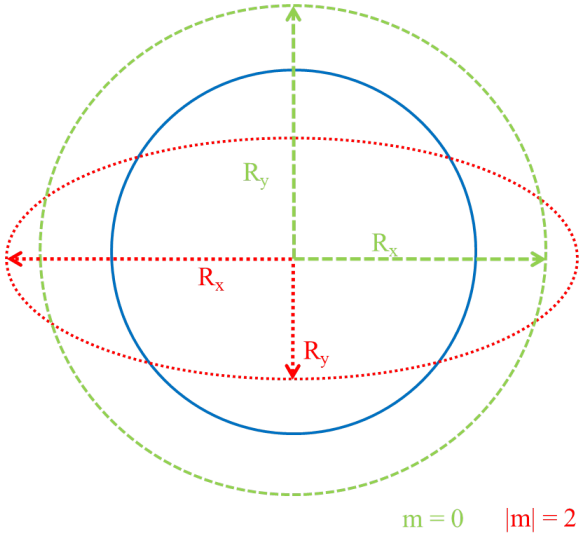

Figure 2.3: Deviations from the equilibrium droplet-form for mode $m = 0$ (green, dashed circle) and $|m| = 2$ (red, dotted ellipse). Two perpendicular radii are shown for each mode respectively. Mode $m = 0$ reveals no angular dependence, as the radius remains constant for all angles. Hence $R_- = 0$. Also mode $|m| = 2$ displays a characteristic feature when summing up R_x and R_y: The $|m| = 2$ radii add up to a constant value. The illustration is based on [6].

The modes $m = 0$ and $|m| = 2$ reveal a characteristic pattern in the R_+ and R_- spectra. As demonstrated in figure 2.3 R_- is equal to zero for $m = 0$ because of the rotational symmetry of the drop shape. As a result the peak corresponding to this mode vanishes in the R_- spectra. The R_+ and R_- spectra are displayed in figures 2.4 and 2.5 respectively. A comparision of these spectra clearly demonstrates the absence of the $m = 0$ peak in the R_- spectrum. In contrast, peaks associated with the $m = 2$ mode are not visible in the R_+ spectra. This is due to the constant value of R_+, which then does not yield a non-zero frequency in the FFT. The mathematical proof can be found in [11].

Figure 2.6 displays the FFT of the number of pixels assigned to the droplet's surface area of a Fe-90% Ni-10% specimen. All five surface oscillation frequencies can be seen. From equation 2.1.1 it becomes apparent, that the distance between the $|m| = 2$ peaks is expected to be twice the distance between the $|m| = 1$ peaks. This knowledge also facilitates a peak assignment. A satisfying agreement between experiment and theory is reached in this

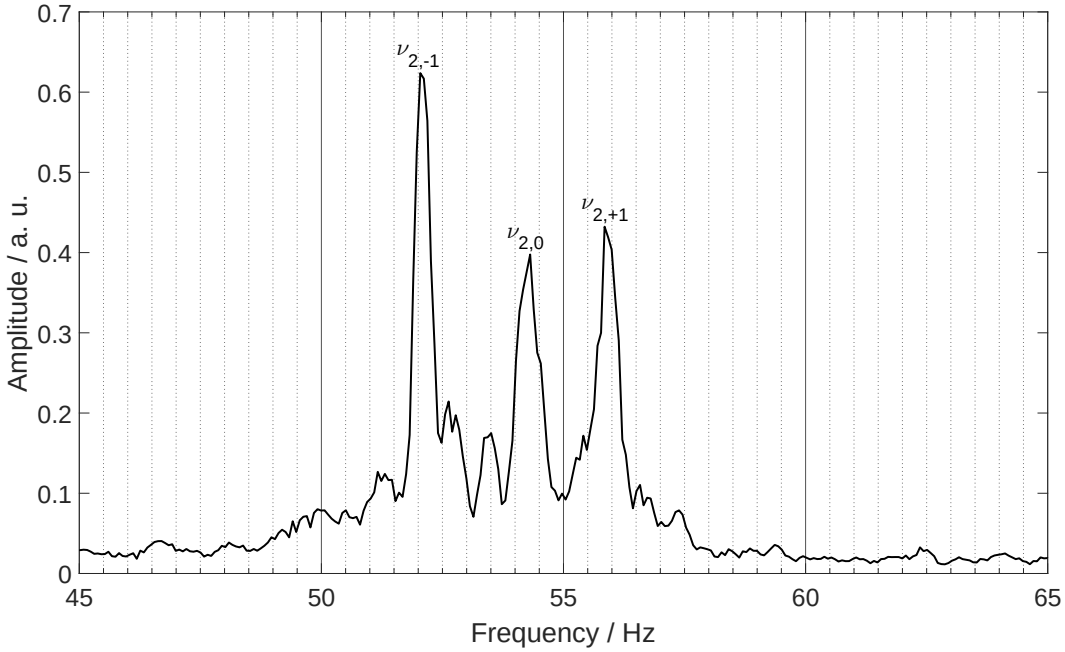

Figure 2.4: R_+ spectrum of Fe-90% Ni-10%: Two perpendicular radii R_x and R_y add up to a constant value for oscillations of the $|m| = 2$ mode. Hence, its Fourier transform yields zero and this peak vanishes in the R_+ spectrum.

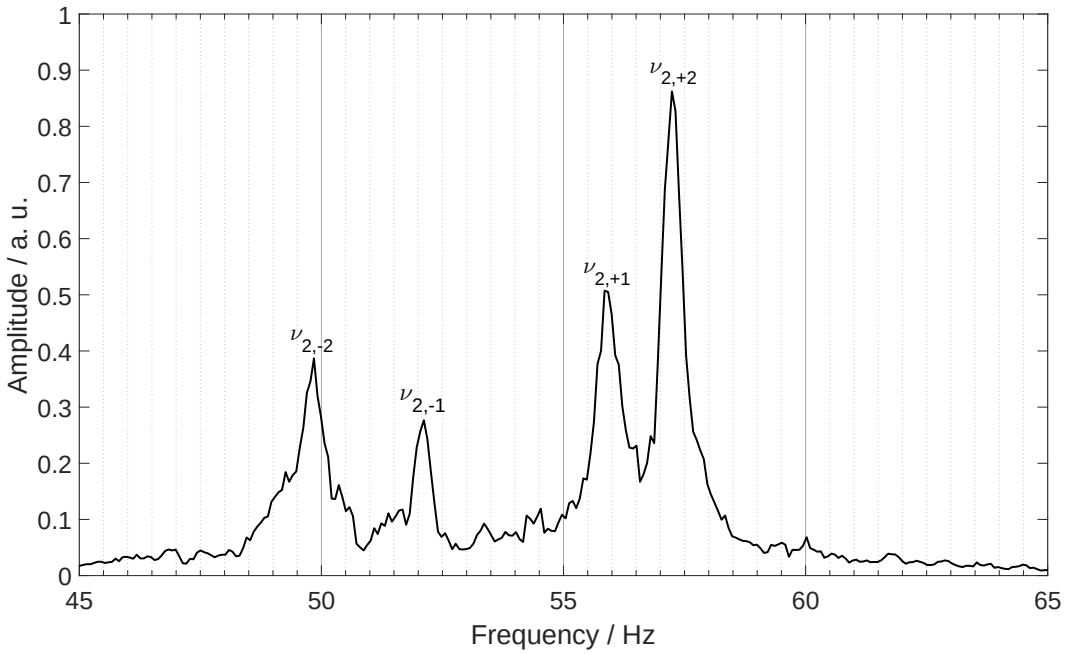

Figure 2.5: R_- spectrum of Fe-90% Ni-10%: Oscillations with $m = 0$ show a rotational symmetry due to their angular independence, therefore $R_x = R_y$. As $R_- = R_x - R_y = 0$, the $m = 0$ peak cannot be seen in the R_- spectrum.

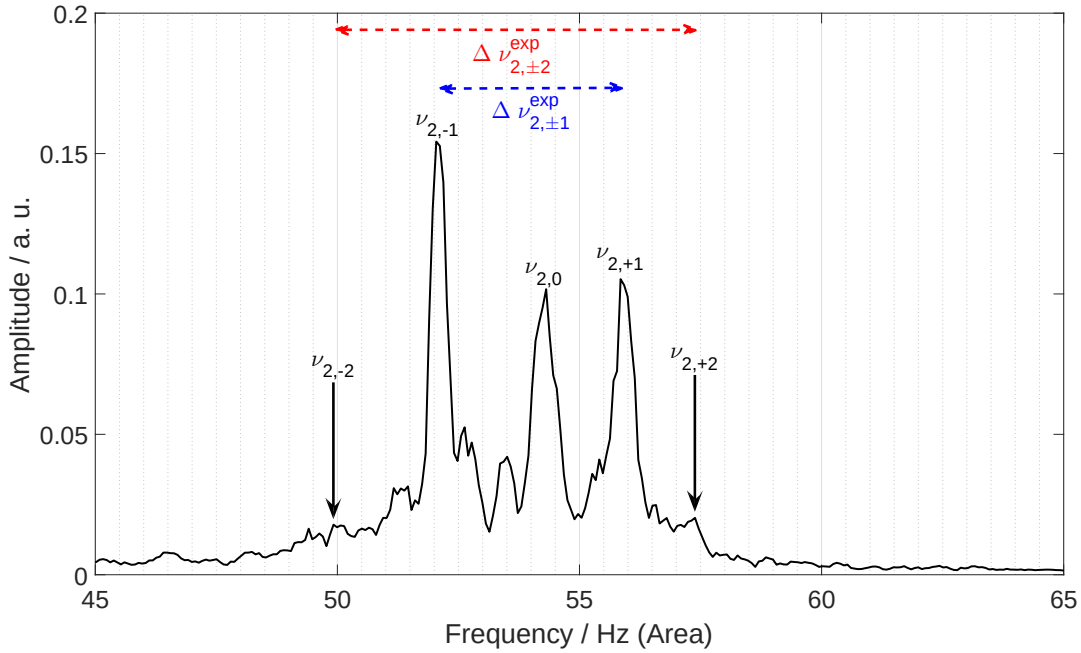

Figure 2.6: Area-spectrum of Fe-90% Ni-10%: The area spectrum represents the change in pixels associated to the droplet's surface. All five peaks needed for the surface density determination are labelled. The three strongly visible peaks are linked to the oscillation modes $\nu_{2,0}$ and $\nu_{2,\pm2}$. By contrast, the peaks related to mode $|m| = 2$ are hardly observable, because of the relatively small change in the surface area. For a reliable peak assignment, further conclusions have to be drawn from the R_+ and R_- spectra.

example as

$$\begin{aligned} \Delta\nu_{2,\pm2}^{exp} &= (7.5 \pm 0.2)\,\text{Hz} \\ \Delta\nu_{2,\pm2}^{theory} = 2 \cdot \Delta\nu_{2,\pm1}^{exp} &= 2 \cdot (3.8 \pm 0.2)\,\text{Hz} = (7.6 \pm 0.6)\,\text{Hz}\ . \end{aligned} \tag{2.24}$$

The area spectrum can give a further hint facilitating a clear peak assignment: The time evolution of the area in the top view is expected to have a high amplitude for modes $m = 0$ and $|m| = 2$. In contrast, the oscillation modes $|m| = 2$ are not associated with a significant surface area change and should therefore, not be visible in this spectrum.

For a better readability, the data of figures 2.4, 2.5 and 2.6 were smoothed with a moving average algorithm of $n = 5$ data points.

CHAPTER 3

Experimental method

3.1 Setup

The electromagnetic levitation device was setup during a research project[4] by the thermophysics and metalphysics group of Graz Universtiy of Technology. Meanwhile, this system allows a parallel measurement of surface tension as well as density of liquid metals/alloys. Figure 3.1 depicts the EML setup used at the TU Graz. The vacuum chamber is equipped with three windows, two along the horizontal axes and one on the top. The sample is placed on a sample holder through the opened front window. The holder, which is operated via a linear feedthrough, is moveable along the vertical axes, enabling a positioning of the metal probe between the coils before levitation. The camera for the density measurement takes shadow-graph pictures from the front side. Therefore, a back-lighting LED-panel, which illuminates the levitated probe through the back-window, is mounted at the backside and an interference filter is placed in front of the camera in order to increase the edge-sharpness of the droplet image. The third window is needed to record the surface oscillations with a second camera by taking pictures along the vertical axes. This camera is positioned on top of the chamber. More information on the imaging system can be found in subsection 3.2.1. Both image acquisition systems are connected to a data processing and analysing unit. Two pyrometers, also coupled to the processing system, record the sample's radiation, which then provides the temperature data. This is explained in more detail in subsection 3.2.2. As a result, the density as well as the surface tension are recorded as a function of

[4] FWF Project P 23838-N20: "Levitation - Measurement of surface tension and density by means of levitation"

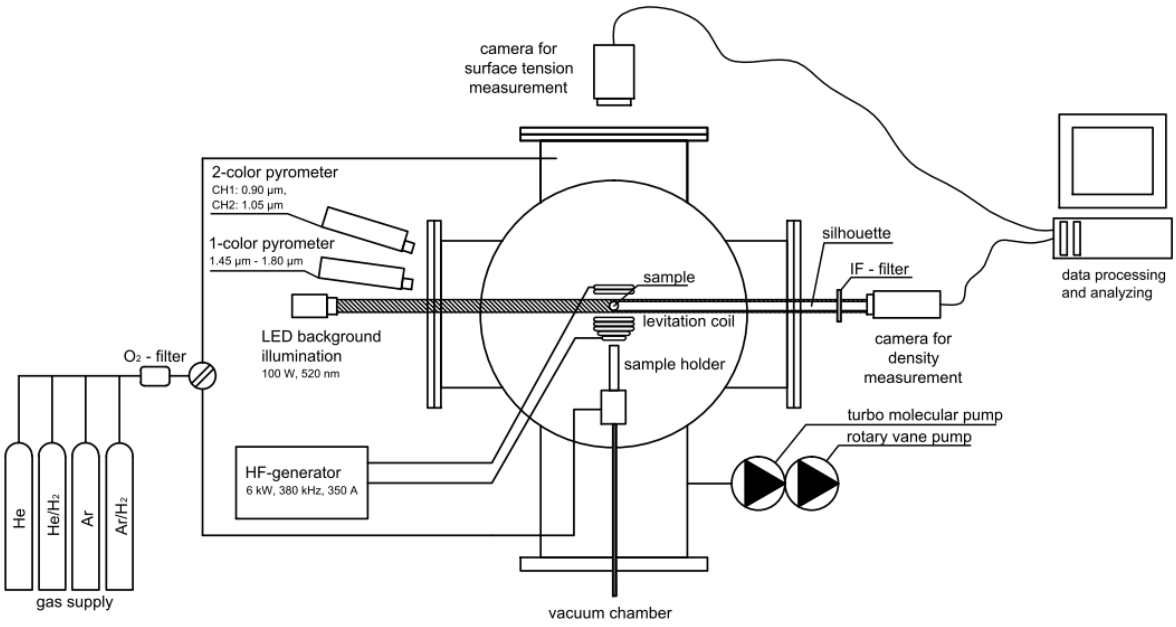

Figure 3.1: Illustration of the experimental setup for surface tension measurement. Source of image: [3], adopted by [4].

temperature. The high-frequency generator (technical information can be found in subsection 3.1.2) in combination with the levitation coil, which is described in subsection 3.1.1, are needed for the levitation as well as the heating of the specimen. The heat dissipation from the specimen to the surrounding is mainly controlled by the gas atmosphere as well as with the help of a gas current through the sample holder onto the specimen (subsection 3.1.4). The vacuum system is elaborated in subsection 3.1.3.

3.1.1 Levitation coil

One of the principal components of electromagnetic levitation setup is the levitation coil. An alternating current supplied by a high frequency generator (for technical information see 3.1.2) is passed through the coil. Therefore, to prevent any melting the levitation coils are cooled with tap water. The coil consists of a hollow pipe. Its windings form an upper and a lower component with electric currents flowing in the opposite direction. Both parts are aligned coaxially. A typical levitation coil design, used for experiments carried out within this thesis, is presented in figure 3.2. For a stable levitation, the coil's design (number of windings and arrangement), position and spacing between windings have to be adapted for each specimen material and weight.

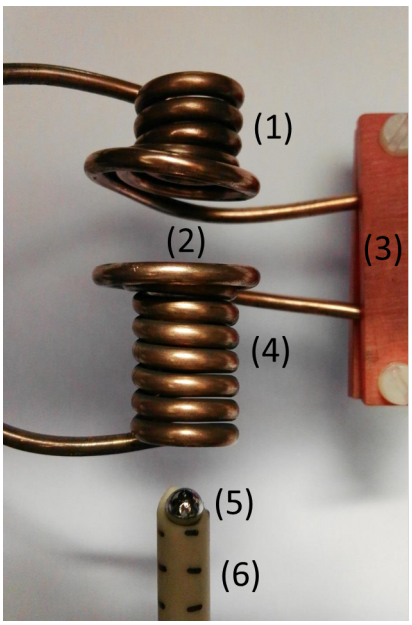

Figure 3.2: Picture of a typical levitation coil (copper tube with outer diameter 3 mm and inner diameter 1.5 mm) used for experiments within this thesis: **(1)** upper windings, **(2)** levitation position of specimen, **(3)** fixation plate for easier coil adaptation, **(4)** (oppositely winded) lower windings, **(5)** specimen (after experiment), **(6)** probe holder made out of aluminium oxide Al_2O_3.

3.1.2 Frequency generator

A frequency generator[5] with a nominal power output of 6 kW creates an alternating current with a frequency around 380 kHz, a voltage of 400 V and an amperage of 350 A [4]. In contrast to the levitation coil, the radio frequency generator is cooled down some degrees below room temperature by an external cooling unit[6] using destilled water. For some experiments heating and cooling of the specimens could be achieved to a certain extend by adjusting the output power of the high frequency generator. As investigated in [4], a change in the power control has neither effect on the output voltage nor on the current, but on the duty cycle of the output current. Several duty cycles with varied output power settings are illustrated in figure 3.3. It was observed, that an increase in the power setting, entails a raise in the specimen's average levitation position and temperature. Due to the longer cycle duration, the probe 'feels' a prolonged uplifting but reduced heating power over the time. This observation still has to be proofed.

[5] *IG 5/200HY*, Trumpf Hüttinger GmbH + Co. KG, Freiburg, Germany

[6] *Kühlmobil* 141, Van der Heijden-Labortechnik GmbH, Dörentrup, Germany

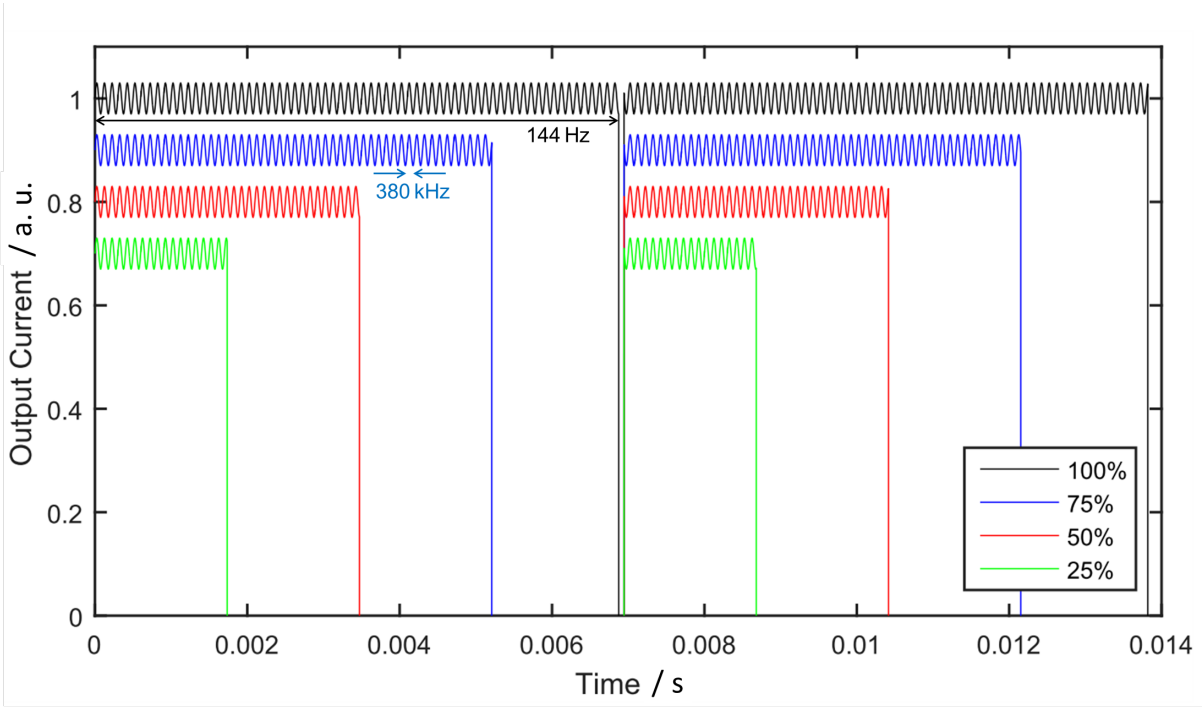

Figure 3.3: Exemplary presentation of different duty cycles of the high frequency generator. The time span of the output pulse can be varied by the power control of the generator. In this figure, five different durations are shown. A nearly continuous signal is only produced at maximum power. The mismatch in the output current value allows a better readabilty and has no physical meaning. The output current is clocked with approximately 380 kHz. For clarity reasons it has been plotted with a 10 kHz periodic signal. Figure adapted from: [4]

.

3.1.3 Vacuum system

Reactions of the liquid metal with oxygen would lead to unwanted surface oxides. In order to prevent oxidation, the experiment has to be executed under vacuum or a protective atmosphere. The levitation coil is located inside a vacuum chamber. Prior to floating the chamber, the system is evacuated. A rotary vane pump[7], which acts as a pre-vacuum pump for a turbo-molecular pump[8], reduces the pressure to approximately 10^{-2} mbar. Subsequently, the pressure is reduced down to 10^{-6} mbar. The turbo-molecular pump is switched off, before floating the housing with an inert gas, whereas the rotary vane pump remains turned on. If the pressure exceeds a pre-set value, a two-port solenoid valve opens and the rotary vane pump reduces the pressure until the set-point is reached again. This enables the maintenance of a constant pressure. For this studies the pre-set pressure point was $p_{pre-set} = 840$ mbar. A high set-point prolongs the cooling range for indirect cooling in which the thermal conductivity is changed by varying the gas components of the chamber. On the other hand, an overpressure due to a delayed opening of the valve needs to be prevented. Therefore, the chosen set-point is the highest possible for this setup which still allows a safe operation.

3.1.4 Gas supply

Because of the increased free path length in vacuum, the occurrence of electric sparcovers between the coil windings becomes more likely. To prevent this from happening, a filling with an inert gas is required (see section 3.1.4). After the evacuation process, which is described in more detail in section 3.1.3, the vacuum chamber is filled with an inert gas mixture. Four gas cylinders, containing different types of gases, are connected to the vacuum chamber via gas pipes. Following gases are used: helium[9], argon[10], ARCAL 10[11] and a custom gas mixture[12]. Besides hampering flash-overs, the gas is used to control the temperature of the sample. Convective heat loss can be regulated to a certain extend by the ratio of the different gases used to fill the chamber. Adjusting the output power of

[7] *Pfeiffer Balzers Duo 0016B*, Pfeiffer Vacuum GmbH, Asslar, Germany

[8] *Pfeiffer Balzers TPU 330*, Pfeiffer Vacuum GmbH, Asslar, Germany

[9] Helium N60; Impurities [ppmv]: $N_2 < 0.5$, $H_2O < 0.5$, $O_2 < 0.5$, Hydrocarbon < 0.5, Ne < 0.5, $H_2 < 0.5$

[10] Argon N50; Impurities [ppmv]: $N_2 < 5.0$, $H_2O < 3.0$, $O_2 < 2.0$, Hydrocarbon < 0.5

[11] ARCAL 10: Ar + 2.4 Vol.% H_2; Impurities [ppmv]: $N_2 \leq 80$, $H_2O \leq 40$, $O_2 \leq 20$

[12] Custom gas mixture: He + 4 Vol.% H_2; Impurities [ppmv]: $N_2 \leq 20$, Ne ≤ 10 $H_2O \leq 5.0$, $O_2 \leq 5.0$, Hydrocarbon < 1.0

the generator also has an effect on the specimen's temperature (for additional information see subsection 3.1.2). A further reduction in temperature is achieved by directing a gas flow onto the specimen. This has to be done with great attention in order not to push the levitating sample out of the stable position. A gas purification unit[13] which removes oxygen is placed between gas container and gas pipes in order to restrict the formation of unwanted surface oxides.

3.2 Measurements

3.2.1 Surface imaging

The image acquisition system consists of two cameras[14] taking pictures with a high frequency, from the top view for surface tension and from the side view for density measurements. Both cameras are linked to a frame-grabber card[15], which is installed in the data processing computer. Currently, the top view camera[16] works with a CMOS detector and allows an image acquisition of 506 fps at full resolution (1280 px times 1024 px) and faster at lower resolution. The Nyquist-Shannon sampling theorem states, that at this sample rate, periodic signals with a maximum frequency of approximately 250 Hz can be resolved. In contrast, the side view camera[17] is equipped with a CCD detector with a maximum frame rate of 120 fps at full resolution (1024 px times 1024 px), thus a recording of oscillations with maximum frequency of 60 Hz is possible. By adjusting the resolution to the needed image size, the maximum sample rate can be strongly increased for the surface tension measurement. Due to the detector properties, the sample rate of the CCD detector cannot be used for surface tension measurements, as the recorded frequency range would not cover the frequencies caused by the surface oscillations of the investigated materials. The density is evaluated with the help of the side-view silhouette images by calculating the volume, assuming rotational symmetry. In addition with the weighed mass, precise density determinations of the metal/alloy in the liquid phase are possible.

[13] ALPHAGAZ PURIFIER Laboratory, AIR LIQUIDE Deutschland GmbH, Düsseldorf

[14] Macro lens: AF Micro-Nikkor ED 200 mm f/4 D IF, Nikon Corporation, Tokio, Japan

[15] Matrox Radient eCL, Matrox Electronic Systems Ltd., Dorval, Canada

[16] EoSens® CL, Mikrotron GmbH, Unterschleissheim, Germany

[17] Basler 1000-120km, Basler AG, Ahrensburg, Germany

3.2.2 Temperature

The optical temperature determination is realised with a single-color pyrometer[18] operating in a temperature range of (250 - 2500) °C and a spectral range of (1.45 - 1.80) μm. The pyrometer converts the detected thermal radiation j into a temperature signal T. The underlying principle is explained by the Stefan-Boltzmann law,

$$j = \varepsilon \sigma T^4 \tag{3.1}$$

with σ, the Stefan-Boltzmann constant and ε, the emittance of the object. Unfortunately, the emissivities of the investigated samples are unknown prior to the experiment. To circumvent this problem, the specimen is assumed to have black body radiation properties in the first step. Therefore, ε is set equal to 1 during the measurement procedure. As a result, the pyrometer detects the so-called 'black temperature' T_{meas}, which has to be corrected in the second step. This can be done under the assumption of a constant, non-temperature dependent emittance in the liquid phase. Then, the real temperature can be evaluated through a calibration of the pyrometer at a reference temperature: During the melting and solidification process a characteristic radiation-temperature behaviour can be seen. At the melting temperature, or solidus/liquidus temperature for alloys respectively, a plateau, similar to the one shown in figure 3.4, becomes visible in the temperature-time plot. The reading-out of this temperature is explained in subsection 3.4.3. Subsequently, the value of the emittance ε_{corr} (equation 3.2) is determined with the help of the measured temperature at the plateau T_m, as well as the corresponding real, reference temperature T_r [12],

$$\varepsilon_{corr} = \exp\left\{\frac{c \cdot h}{k \cdot \lambda}\left(\frac{1}{T_r} - \frac{1}{T_m}\right)\right\} \tag{3.2}$$

$$T_{corr} = T(\varepsilon_{corr}) = \left(\frac{1}{T_{meas}} + \frac{c \cdot h}{k \cdot \lambda}\ln(\varepsilon_{corr})\right)^{-1} \tag{3.3}$$

Recalculating the 'black temperature' graph with the corrected emittance as input parameter of formula 3.3, yields the true temperature values T_{corr}. The speed of light is denoted with c (299 792 458 ms^{-1}), the Planck constant with h ($6.626068 \cdot 10^{-34}$ Js^{-1}) and the Boltzmann constant with k ($1.38065 \cdot 10^{-23}$ JK^{-1}). These values are taken from [13]. The centre of the one-wavelength pyrometer is supposed to be at $\lambda = 1.625\,\mu$m.

[18] IMPAC IGA 6 Advanced, LumaSense Technologies, Frankfurt/Main, Germany

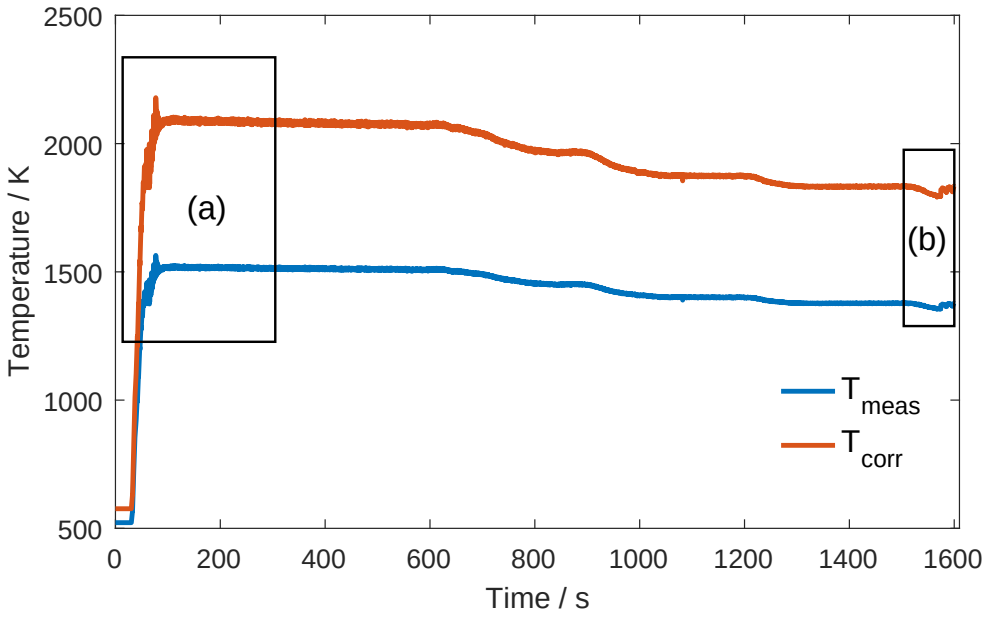

Figure 3.4: Temperature versus time profile of iron measurement: The T_{meas}-plot represents the 'black temperature' of the iron specimen measured with a commercial pyrometer. The second temperature gradient T_{corr} represents the real temperature profile determined by calibrating the pyrometer at the melting plateau. Inset 3.5a frames the time period of the melting process, whereas inset 3.5b focusses on the solidification plateau.

An ab initio temperature signal would facilitate the experimental process. For this reason, a so called 2-color ratio pyrometer[19] has been installed. This pyrometer operates at the wavelengths 0.9 μm and 1.05 μm. Due to this principle of operation, no emittance-evaluation is needed for this type of pyrometer. At this stage, temperature data, measured with this pyrometer, should only be used as an estimation for the temperature of the specimen. The the temperature-time graphs recorded during the experiments showed a relevant distinction between the measured temperature of the 2-color ratio pyrometer and the corrected one of the single color pyrometer. The reliability of this newly installed pyrometer needs further investigation (see [14]).

[19] ISR 6-TI Advanced, LumaSense Technologies, Frankfurt/Main, Germany

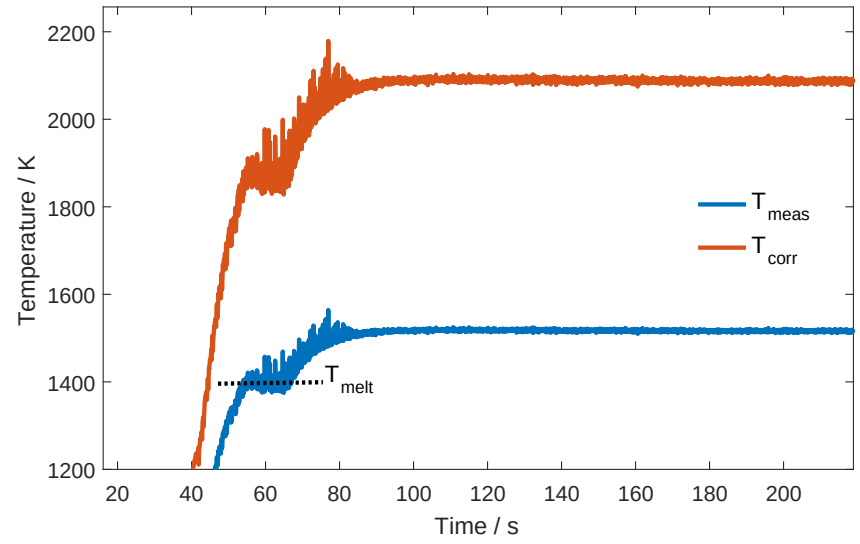

(a)

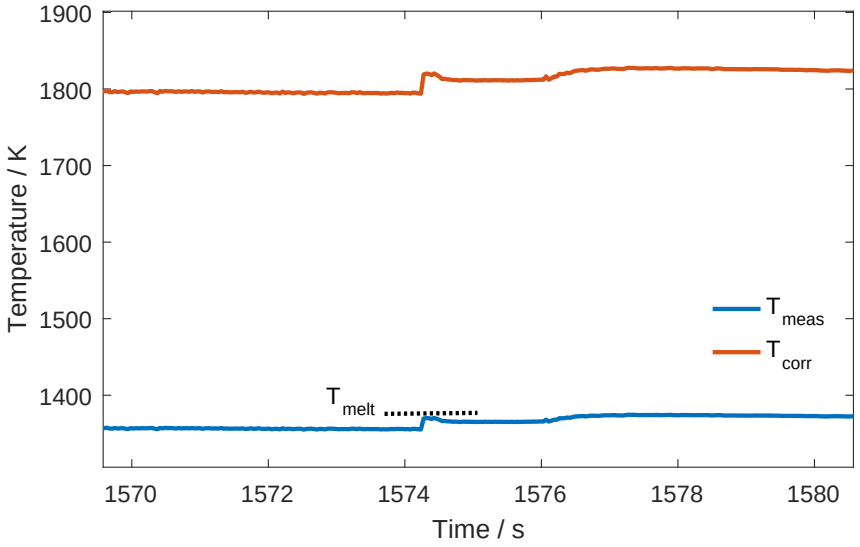

(b)

Figure 3.5: 'Black temperature' T_{meas} as well as recalculated real temperature T_{corr} profile plotted as a function of time: Additionally the melting/solidification plateau has been marked (denoted with T_{melt}) in figure (a)/(b). The reference melting temperature for iron is 1811 K [15]. The temperature at the melting point has to be estimated with a higher uncertainty than at the solidification point due to the noisier signal. For that reason, the temperature of the latter plateau was preferably taken as reference temperature for pyrometer calibrations: (a) A decline in the radiation signal while the heating process marks the melting point. The melting temperature for iron was assessed to be at approximately (1842±6) K in this experiment. The signal at the melting plateau appears to be noisier than at the solidification plateau. This is taken into account in a higher uncertainty. (b) Also the transition from liquid to solid is clearly visible in the temperature signal. During the cooling process, undercooling followed by solidification of the iron creates a step in the temperature graph. The solidification temperature for iron is reached at around (1820 ± 2) K.

3.3 Procedure

The iron-nickel samples were taken from cuboid casting samples by cutting them off with a handsaw. If relevant contaminations due to e.g. the sample preparation process was suspected, the cutting was done with a turning machine. All probes were cleaned in an ultrasonic bath[20] in a vial containing pure acetone for at least 10 minutes. For clarification reasons, a composition analysis of some samples with energy dispersive X-Ray spectroscopy was done. The mass of each specimen was then measured with a precision balance[21]. To determine the weight loss due to evaporation during the liquid phase, the specimens were weighed again after the experiment. The samples were placed on the sample holder and after closing the front window, the rotary vane pump, followed by the turbo molecular pump (details about the vacuum system can be found in 3.1.3) generated a high vacuum. The probe chamber was flooded with an inert gas, or a combination of inert gases, depending on the material's heat radiation properties (for explanation, see subsection 3.1.4). The specimen was positioned between the levitation coils in the expected floating spot, and the high-frequency generator turned on. The levitated sample melted and heated up till heating power and heat dissipation were balanced. The physical effects created by the magnetic field of the levitation coil are elaborated in section 2.1. The cooling or heating process of the probe was piloted with the help of pressure, gas composition and/or generator power. The temperature was measured with one- and two-color pyrometers, which are explained in 3.2.2, and the temperature-time gradient was collected. At a stable temperature point, images of the surface oscillations and shadow-graph images were recorded with the high-speed cameras (see subsection 3.2.1) for various temperature points. To obtain a low signal-to-noise ratio, focus, shutter time, frame-rate etc. were adjusted. For the investigated materials it was not possible to use fixed values for the parameters mentioned before. Therefore, they had to be optimized for each experiment. The measurements showed, that for the investigated materials, recordings of 4100 to 8200 images with a frame-rate around 300 fps were a good trade-off between reliable frequency spectra with a high enough resolution and short recording times. The duration of a recording is limited due to material evaporation and temperature fluctuations. At the end of the experiment, the liquid specimen was cooled down below the solidification point by a gas flow through the specimen holder. To pick up the still levitating, but already solid sphere, the gas current was turned off and the specimen

[20] EMAG TECHNOLOGIES® EMMI®-20HC, Batch No. Gi376

[21] *METTLER TOLEDO AB104-S-A*, Mettler-Toledo GmbH, Giessen, Germany, balance accuracy 0.1 mg

holder was quickly placed directly below the probe. By decreasing the power of the high-frequency generator, the levitating force is reduced and the specimen could be caught with the holder.

3.4 Evaluation

3.4.1 Image evaluation

The image evaluation was done with a VISUAL C# program written by Aziz [2] and Schmon [3], and extended by Leitner [4]. In case of the surface tension evaluation, the radii of the specimen were measured from the center of mass to the edge in 5 °-steps. Because of the higher demands for density measurements, concerning radius accuracy, an increment of 1 ° and a different edge detection software was used. Density measurement and edge detection software are described in more detail in the literature mentioned above. An ASCII-file, which stores the the crucial information for the frequency spectra, is generated with this program. This file contains the centre of mass coordinates in x- and y-direction CM_x [px] and CM_y [px], number of pixels assigned to the specimen's surface area N_{pix} and the distances from center of mass to detected edge in a direction specified through an angle for each image recorded. Before the improvements in [4], the image evaluation could only be done after the experiment had been finished. Now it is possible to generate an ASCII-file during an ongoing experiment. This in turn, allows a study of the frequency spectra, directly after the necessary data has been recorded at a specific temperature. An ad hoc optimization of various parameters influencing the quality of the spectra, like generator power, number of images recorded, shutter time and so on, has thus become possible already during the experimental process.

3.4.2 Frequency spectra evaluation

The frequency spectra are computed through a FFT of the information drawn from the image evaluation. The coordinates of the center of mass CM_x and CM_y yield the translation frequencies in the horizontal plane, plotted in the frequency spectra labelled $\nu_{t,x}$ and $\nu_{t,y}$. If $\nu_{t,z}$ is not visible in those spectra, it is calculated with equation 2.1.1. The values of two radii perpendicular to each other, transform to the oscillation frequency spectra R_x and R_y. For the determination of the surface tension, the frequency peaks corresponding to the oscillation modes $m \in \{-2, -1, 0, 1, 2\}$ have to be assigned. The relation between surface

tension and those peaks is explained in 2.1.1. To facilitate the process of peak assignment, two additional frequency spectra, denoted with R_+ and R_- are calculated respectively, by adding or subtracting R_x and R_y. A modus operandi for the peak evaluation has been introduced in the subsection 2.1.2.

3.4.3 Surface tension evaluation

The frequency values of the oscillations modes and the translation frequencies obtained through the evaluation of the frequency spectra (evaluation explained in subsection 3.4.2), as well as some other input parameters are needed for the surface tension calculation. The underlying physical concept of this so called oscillating drop method is elaborated in subsection 2.1.1. This function loads a script which contains following informations:

- mass prior and posterior to an experiment
- T_{melt} read out with the help of the melting plateau measured with the one-color pyrometer
- T_{melt} from literature as reference temperature
- Density ρ at the melting point to determine the radius r in formula 2.11

CHAPTER 4

Results and Discussion

For the majority of pure metals, surface tension has already been experimentally acquired. In spite of this, the situation for the larger part of alloys is different: With regard to the iron-nickel system, only few data can be found. Brillo et al. [16] for example, have examined the surface tension of pure iron and nickel, as well as of their binary alloys Fe-75 at% Ni-25 at%, Fe-at 50% Ni-50 at% and Fe-25 at% Ni-75 at%[22] . This work attempts to fill some open gaps in order to provide a more comprehensive overview of the iron-nickel system with respect to this thermodynamic property. In addition to pure iron, investigstions on Fe-90% Ni-10% and Fe-60% Ni-40% have been done in the course of this thesis. The detailed material data for the investigated matter is included in the appendix. The surface tension of nickel has already been measured by the thermo- and metalphysics group of this institute by Aziz et al. [17] and will be included for comparison reasons as well.

Due to the high price of pure iron and in order to gain experimental knowledge, the alloy Fe-90% Ni-10% was measured beforehand: In the expectation of a similar behaviour for iron, working with specimens containing iron in large part, allowed an optimization of the coil set-up and the mass of the sample in advance. In the course of these experiments, an unsatisfying noise-to peak ratio in the surface oscillation frequency spectrum raised difficulties. Therefore, an experimental analysis of the underground signal was performed. Its procedure and outcome are presented in section 4.1. With this extended proficiency, the surface tension of pure iron and subsequently of Fe-60% Ni-40% were measured as well.

[22] for simplicity reasons, atmic weight percent will be denoted as % only

The data points of surface tension vs temperature $\gamma(T)$ are fitted through a linear regression model,

$$\gamma(T) = \gamma(T_m) + \frac{d\gamma}{dT}(T - T_m) \tag{4.1}$$

with $\gamma(T_m)$ being the surface tension of the sample at the liquidus temperature T_m and $\frac{d\gamma}{dT}$ denoting the surface tension change with respect to temperature. These fit parameters are obtained by means of a least squares approach. For each material investigated within this work, the experimental data were fitted with equation 4.1. The resulting linear regression, which is indicated by a solid line, is plotted along with the respective data set in each figure. In contrast, reference values are marked by non-solid lines. In each diagram, a red, dashed, vertical line indicates the material's liquidus temperature. The uncertainty budget for the data points was calculated for each material according to GUM WORKBENCH[23] by the help of the automated evaluation described in [4]. In order to ensure an easier readability, the uncertainty is only plotted for two data points of each material. An exemplary budget, created for pure iron, is elaborated in chapter 5. The results dealing with the surface tension of pure iron and the two alloys Fe-90% Ni-10% and Fe-60% Ni-40% are discussed in sections 4.2, 4.3 and 4.4 respectively. Finally, an overview of the surface tension of the iron-nickel system, including the outcome of this work and literature data, can be found in section 4.5.

4.1 The noise produced by the EML setup

In order to allow an investigation of the noise which is produced by the prevalent EML setup itself, a small adjustment had to be done: The image acquisition system used for surface tension measurements records pictures of specimens emitting thermal radiations. An alternative for the bright specimen had to be found to detect only translation frequencies ν_t produced by system itself. Because the spectra associated with ν_x and ν_y did not show any significant distinction for the conducted experiments, only the x-direction was analysed. Therefore, a white plastic screw was plunged into the tube of the specimen holder and the movement of the bolt head, which was illuminated by a pocket lamp, was evaluated. The influence of the following EML components were systematically investigated: the rotary vane pump with and without vibration damping, the compressor, the water pump (the latter two are part of the cooling system) and the LED panel fan (cooling the back-

[23] Version 2.4.1.388, http://www.metrodata.de/ver24.html

Table 4.1: Frequency signals generated by different components of the EML setup: The uncertainties of the frequencies are estimated with $\Delta\nu_{t,x} = \pm\ 0.2\,\mathrm{Hz}$.

Component	Peak	$\nu_{t,x}$ [Hz]
cold system	(A), (B), (C)	10.9, 25.6, 101.1
LED panel fan	(D)	37.9
rotary vane pump	(E)	45.7
compressor/water pump	(F)	48.0

ground illuminating system which is used for density measurements). Contributions to the frequency spectrum evoked by the rotating fan needed to be investigated as surface tension and density measurements can be recorded simultaneously. Thus, this component can also affect the surface tension experiments.

Figure 4.1 depicts the background noise with all components turned off (this case will be described as 'cold system'). Already in this spectrum, three major peaks, located at approximately $(10.8 \pm 0.5)\,\mathrm{Hz}$, $(25.6 \pm 0.5)\,\mathrm{Hz}$ and $(101.1 \pm 0.5)\,\mathrm{Hz}$ emerge. They are labelled with (A), (B) and (C) respectively in figure 4.1. These spikes also arise in the spectrum with all units turned on ('hot system'), illustrated in figure 4.2. It was possible to clearly assign the three most dominating peaks to a certain source (see table 4.1).

The damping system reduces the dominant rotation vane pump peak by a factor of up to 5. This then facilitates a clear peak assignment, as the peaks resulting from surface oscillations are expected to show a greater amplitude. Therefore, the peak produced by the pump cannot be mistaken for a fundamental frequency so easily, if the vibration damping module is used. Still, oscillations frequencies close to those evoked by the system, should be treated with great caution, as a coupling of those might result in an artificial increase of amplitude or peak broadening.

Thus, with the above in mind, the specimen's weight should be adopted in such a way, that the measured fundamental frequencies are within the frequency range

$55\,\mathrm{Hz} \leq \nu_{2,m} \leq 95\,\mathrm{Hz}$. The range $\nu_{2,m} \geq 105\,\mathrm{Hz}$ should be avoided. There, experiments yielded a bad signal-to-noise ratio. This can be traced back to the decreased specimens' dimensions: As the fundamental frequency is proportional to $\frac{1}{\sqrt{m}}$, the usage of light samples becomes necessary. This leads to a reduction of the surface oscillations amplitude due to the deteriorated detection of changes in the radii and consequently, results in a worse signal-to-noise ratio.

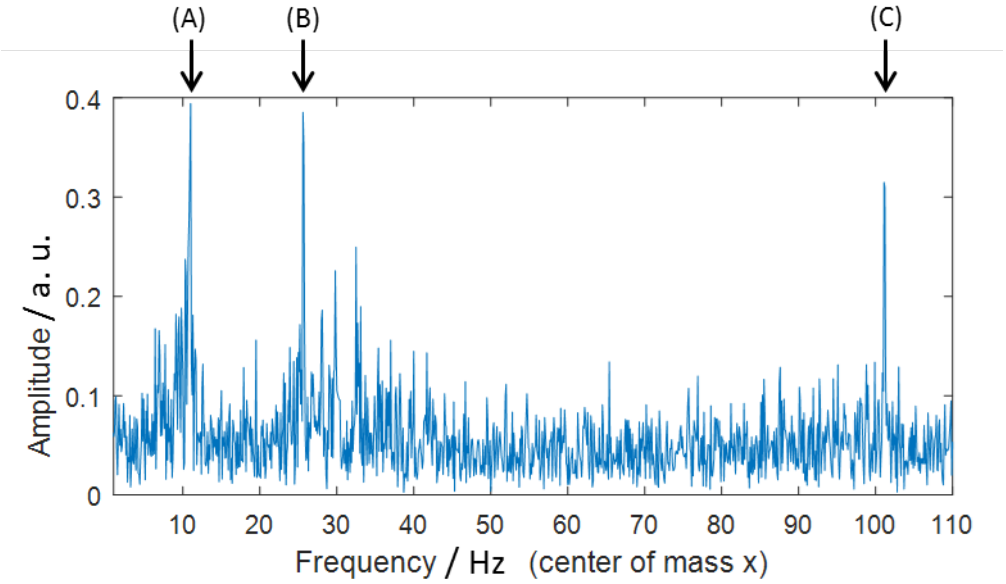

Figure 4.1: 'Cold system' of the EML setup: Even with all investigated components turned off, three main peaks, labelled (A), (B) and (C), can be seen. Their values can be taken from table 4.1.

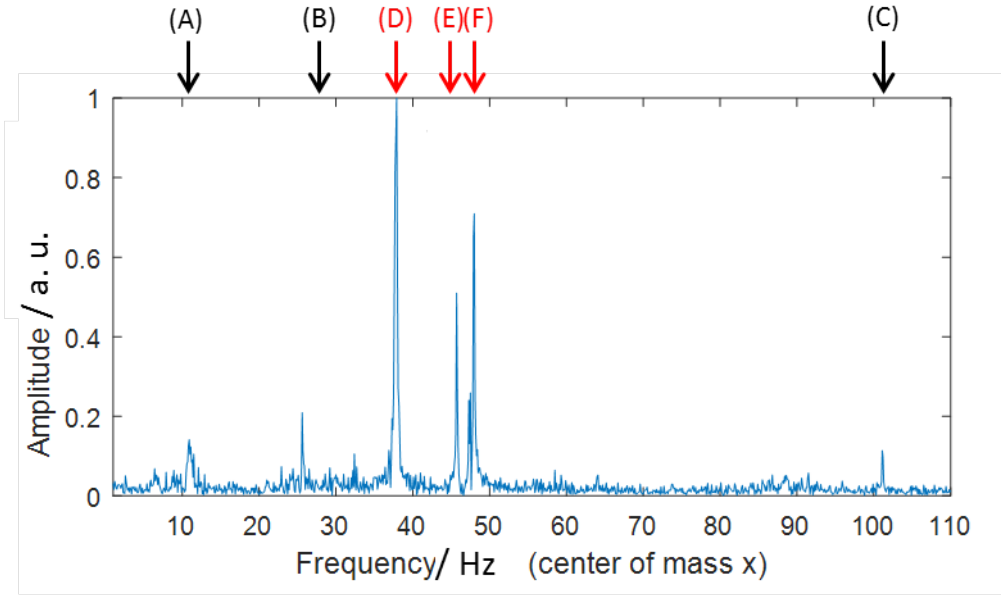

Figure 4.2: 'Hot system' of the EML setup: The spectrum was recorded with the following components turned on: rotary vane pump including vibration damping, compressor, water pump and LED panel fan. Six peaks could be assigned, whereof three ((A), (B) and (C)) were already visible in the spectrum of the 'cold system'. The cause of the remaining other three frequencies (D) to (F), could be traced back to different components of the EML setup and is documented in table 4.1.

4.2 Iron

As most spectra did not allow an easy peak assignment, a lot of effort was taken for experimental improvements, like the the optimization of the coil setup or specimen's mass and the fine tuning of image recording parameters. The most stable levitating position for pure iron samples was obtained by flooding the complete chamber with ARCAL 10[24] and then, replacing some gas content with a custom gas mixture[25], containing helium and hydrogen, for cooling during an ongoing experiment. The frequency generator power output as well as the aperture size had to be adopted at each temperature point. In order to take mass evaporation into account, a decrease of the specimen's mass during the experimental process is presumed. To facilitate matters, it is supposed to be linear. This assumption is incorporated into the surface tension calculation, therefore, the specimen had to be weighed before and after an experiment. Table 4.2 summarizes the masses and their loss.

Table 4.2: Mass of iron specimens: Initial mass m_I ($\Delta m_I = \pm\ 0.1\,\mathrm{mg}$) and final mass m_F ($\Delta m_F = \pm\ 0.1\,\mathrm{mg}$) in addition to the relative mass loss ($\Delta m_{rel} = \pm\ 0.2\,\%$) are given.

m_I [mg]	m_F [mg]	m_{rel} [%]
530.2	523.4	1.3
541.3	535.7	1.0
812.3	803.5	1.1
559.1	548.5	1.9
754.5	743.1	1.5

Figure 4.3 illustrates, that data measured in this work show a good agreement with the experiments done by Brillo and Egry [16] and Brooks et al [18]: The value of the surface tension at the melting temperature of (1878 ± 84) mN·m^{-1} of this work matches very closely the one measured by Brooks et al [18]. Also Brillo and Egry [16], who for example, conducted their experiments under a 92% He and 8% H_2 atmosphere, obtained a surface tension which lies within this error margin. The expected decrease of the surface tension with respect to the temperature can be clearly seen. The discrepancy in the temperature gradient of iron of this work compared to the two publications mentioned before might be due to difficulties related with the formation of surface oxides. This influence is discussed in more detail in chapter 5. It has to be pointed out, that already a comparison of literature

[24] ARCAL 10: Ar + 2.4 Vol.% H_2; Impurities [ppmv]: $N_2 \leq 80$, $H_2O \leq 40$, $O_2 \leq 20$

[25] Custom gas mixture: He + 4 Vol.% H_2; Impurities [ppmv]: $N_2 \leq 20$, Ne ≤ 10 $H_2O \leq 5.0$, $O_2 \leq 5.0$, Hydrocarbon < 1.0

values among themselves show a variance.

Table 4.3: Surface tension of iron as measured by different authors: Temperature at the melting point T_m, temperature range of experiments T_{range}, surface tension at melting point $\gamma(T_m)$, temperature gradient of surface tension $\frac{d\gamma}{dT}$.

T_m [K]	T_{range} [K]	$\gamma(T_m)$ [mN·m^{-1}]	$\frac{d\gamma}{dT}$ [mN·m^{-1}K^{-1}]	Reference
1811 [15]	1810 to 2070	1878 ± 84	$-(0.32 \pm 0.04)$	this work
1811	1800 to 2060	1920	-0.40	[16]
1810	1460 to 1970	1870	-0.43	[18]

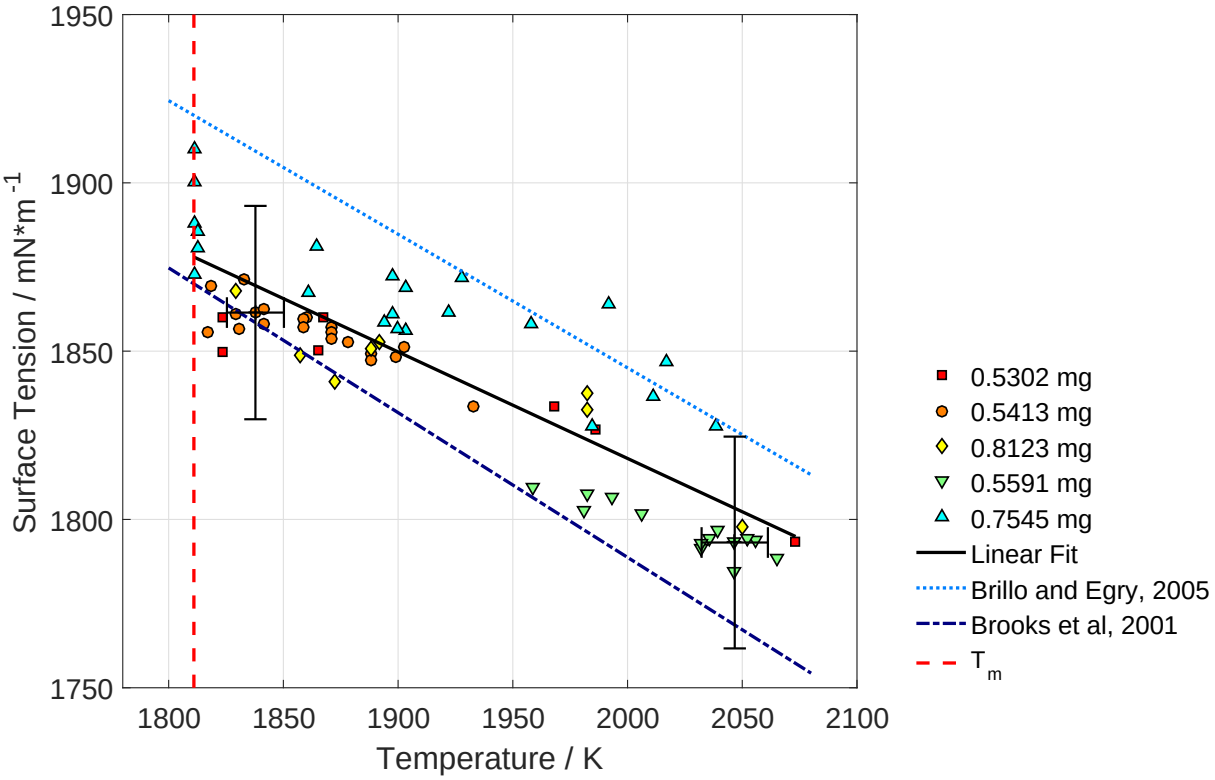

Figure 4.3: Surface tension of iron as a function of temperature: The solid line refers to the linear regression representing the experimental data measured in this work. It shows a satisfying agreement to fits produced by Brillo and Egry [16] and Brooks et al [18].

4.3 Fe-90% Ni-10%

The impact of surface oxides and other contamination on the surface tension strongly influenced many Fe-90% Ni-10%-experiments. Therefore, most of the data collected at the beginning of the series of measurements could not be used and great caution had to be paid

in the preparation part. A gas composition consisting of around 7 parts of ARCAL 10 and 5 parts of the custom gas mixture has turned out to work quite effectively for this type of specimens: The additional helium prevents an excessive mass loss through evaporation, as it helps to reduce the temperature especially in the first part of the experiment. In addition the hydrogen in the mixture acts as a reducing agent suppressing oxidation of the melt surface. Mass and fit parameters of Fe-90% Ni-10% are presented in the tables 4.4 and 4.5. The experimental in figure 4.4 are shown together with the linear regression based on 4.1.

Table 4.4: Mass of Fe-90% Ni-10% alloy specimen: Initial mass m_I ($\Delta m_I = \pm\, 0.1\,\mathrm{mg}$) and final mass m_F ($\Delta m_F = \pm\, 0.1\,\mathrm{mg}$) in addition to the relative mass loss ($\Delta m_{rel} = \pm\, 0.2\,\%$) are given.

m_I [mg]	m_F [mg]	m_{rel} [%]
589.5	577.7	2.0
386.2	384.2	0.5
494.9	484.9	2.0
529.5	524.8	0.9

Table 4.5: Surface tension of Fe-90% Ni-10%: Temperature at the melting point T_m, temperature range of experiments T_{range}, surface tension at melting point $\gamma(T_m)$, temperature gradient of surface tension $\frac{d\gamma}{dT}$.

T_m [K]	T_{range} [K]	$\gamma(T_m)$ [mN·m^{-1}]	$\frac{d\gamma}{dT}$ [mN·m^{-1}K^{-1}]
1783 [19][26]	1755 to 2060	1714 ± 155	$-(0.12 \pm 0.08)$

[26] as cited in [20]

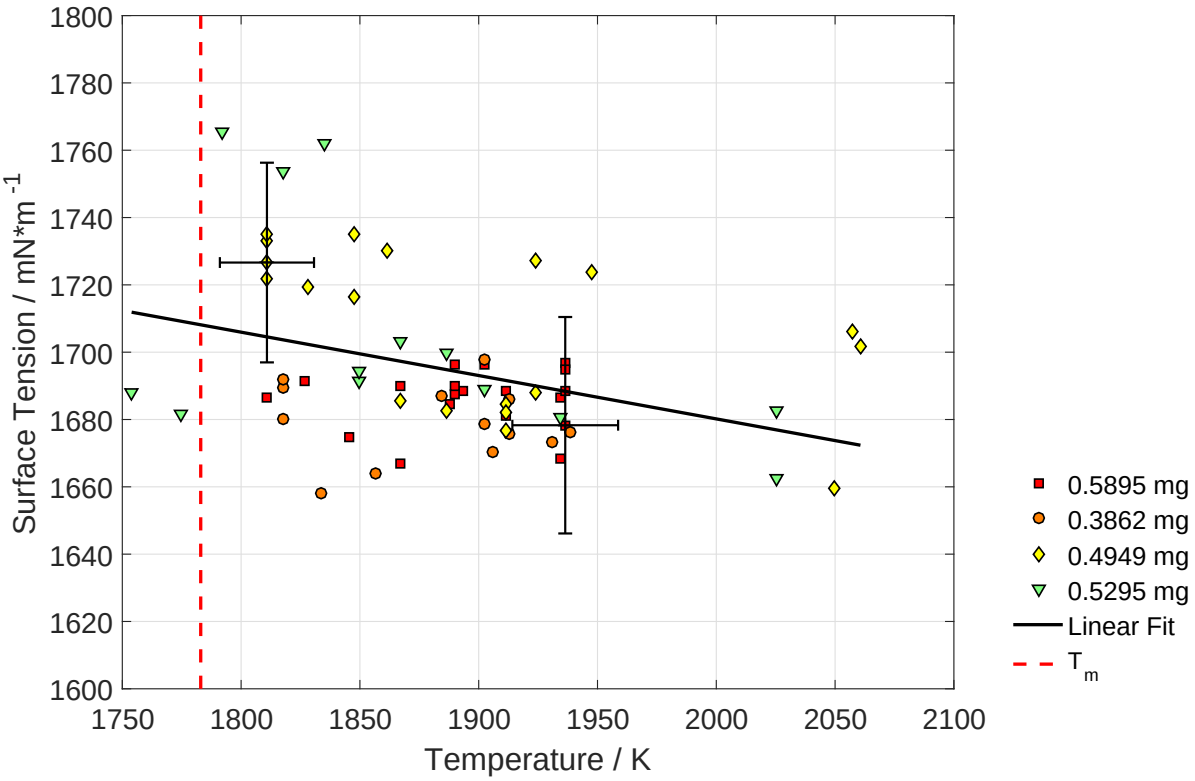

Figure 4.4: Surface tension of Fe-90% Ni-10% as a function of temperature: The data could not be plotted in comparison with other publications as no reference values could be found.

4.4 Fe-60% Ni-40%

The Fe-60% Ni-40%-cast was provided by Böhler. It is only the first of several different iron-nickel alloys produced by our project partner which was to be investigated on its surface tension-temperature dependence. A particularly flat regression was found for this material. For the vast majority of the experiments conducted on this material, a ratio of approximately 1:1 between ARCAL 10 and the custom gas mixture was used. The cooling was, as for all other materials, done with the latter. The distribution of the data might be explained to certain extend by a difference in the vacuum quality prior to the flooding (details on the vacuum can be found in 3.1.3). Similar to the Fe-60% Ni-40%, no investigations on this alloy could be found in the literature.

Table 4.6: Mass of Fe-60% Ni-40% alloy specimen: Initial mass m_I ($\Delta m_I = \pm\, 0.1\,\mathrm{mg}$) and final mass m_F ($\Delta m_F = \pm\, 0.1\,\mathrm{mg}$) in addition to the relative mass loss ($\Delta m_{rel} = \pm\, 0.2\,\%$) are given.

m_I [g]	m_F [g]	m_{rel} [%]
464.1	458.9	1.1
513.8	505.7	1.6
559.9	553.6	1.1
653.0	642.0	1.7
501.8	497.4	0.9
512.5	506.9	1.1

Table 4.7: Surface tension of Fe-60% Ni-40%: Temperature at the melting point T_m, temperature range of experiments T_{range}, surface tension at melting point $\gamma(T_m)$, temperature gradient of surface tension $\frac{d\gamma}{dT}$.

T_m [K]	T_{range} [K]	$\gamma(T_m)$ [mN·m^{-1}]	$\frac{d\gamma}{dT}$ [mN·m^{-1}K^{-1}]
1725 [21]	1725 to 1965	1624 ± 171	$-(0.07 \pm 0.06)$

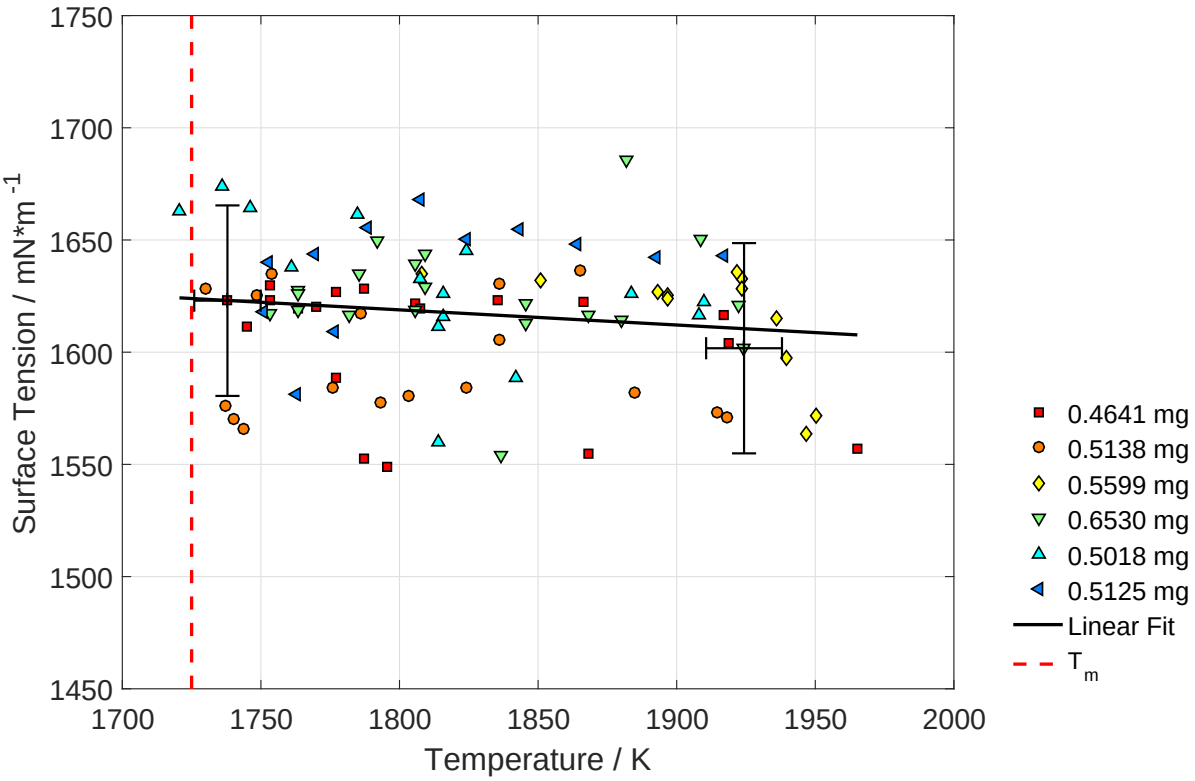

Figure 4.5: Surface tension of Fe-60% Ni-40% as a function of temperature: The linear regression yielded a relatively small temperature gradient for this alloy. Again, no reference data were available.

4.5 Iron-nickel system

This section provides an overview of the surface tension measured within the framework of this thesis and of some literature values.
The parameters $\gamma(T_m)$ and $\frac{d\gamma}{dT}$ obtained by the least squares fit of equation 4.1, are summarized in table 4.8 together with the materials' respective liquidus temperatures. T_{range} describes the temperature range within which the measurements were conducted. Figure 4.6 allows a visual comparison of the results, by showing the regressions lines basing on equation 4.1 with the parameters below.

Table 4.8: Surface tension of the iron-nickel system: Surface tension at the liquidus point $\gamma(T_m)$ and its temperature gradient $\frac{d\gamma}{dT}$ for pure iron and the alloys Fe-90% Ni-10%, Fe-60% Ni-40% in the liquid phase were measured in this work. Further listed are temperature at the melting point T_m, as well as the temperature range of experiments T_{range}. In order to allow a comparison, these values are summarized along with reference data in this table.

Material [at%]	T_m [K]	T_{range} [K]	$\gamma(T_m)$ [mN·m^{-1}]	$\frac{d\gamma}{dT}$ [mN·m^{-1}K^{-1}]	Reference
Fe	1811 [15]	1810 to 2070	1878 ± 84	$-(0.32 \pm 0.04)$	this work
Fe	1811	1800 to 2060	1920	-0.40	[16]
Fe	1810	1460 to 1970	1870	-0.43	[18]
Fe-90% Ni-10%	1783 [19][27]	1755 to 2060	1714 ± 155	$-(0.12 \pm 0.08)$	this work
Fe-75% Ni-25%	1746	1740 to 1860	1930	-0.173	[16]
Fe-60% Ni-40%	1725 [21]	1725 to 1965	1624 ± 171	$-(0.07 \pm 0.06)$	this work
Fe-50% Ni-50%	1713	1650 to 2030	1910	-0.33	[16]
Ni	1728	1700 to 2020	1864 ± 3	$-(0.35 \pm 0.02)$	[17]
Ni	1728	1290[28] to 2020[29]	1797	-0.15	[22]

Butler [23] formulated a theoretical concept, the so-called Butler model, which allows a prediction of the surface tension of liquid alloys. Brillo et al [24] applied Butler's equation to binary alloys. Figure 4.7 illustrates the surface tension of liquid iron-nickel as a function of the nickel concentration at 1773 K. Pure iron shows the highest, and pure nickel the lowest surface tension in measurements at this temperature. According to the Bulter model, this value decreases with an increasing amount of nickel. In order to allow a comparison with this theoretical model, the surface tension of pure iron as well as of the alloys Fe-90% Ni-10%, Fe-60% Ni-40% at this specific temperature were calculated and are also marked in this figure. The convex curve is a result of the prohibited nickel segregation to the outer

[27] as cited in [20]

[28] laboratory: National Physics Laboratory

[29] laboratory: Deutsches Zentrum für Luft- und Raumfahrt

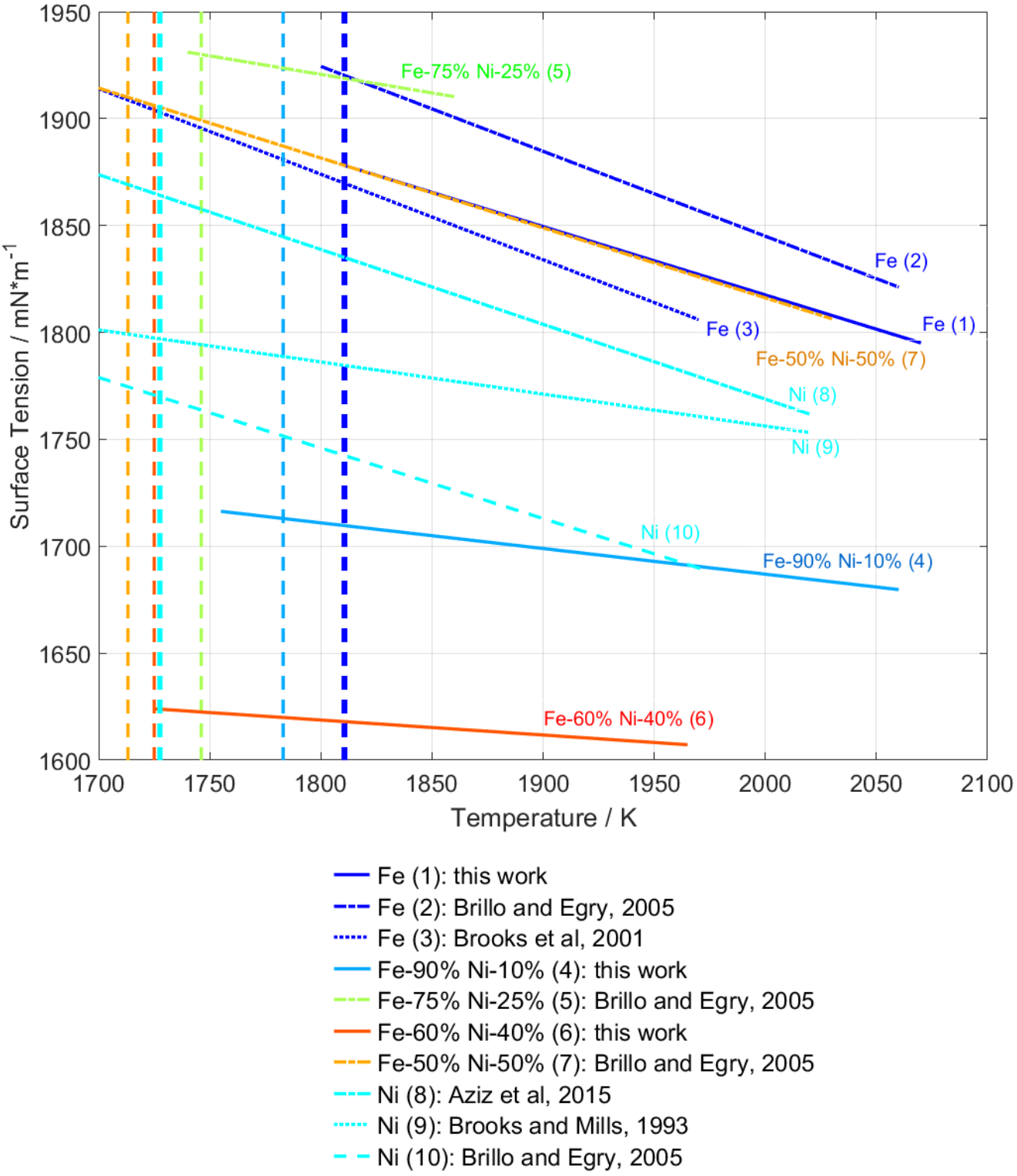

Figure 4.6: Surface tension of the liquid iron-nickel system as a function of temperature: The surface tension-temperature dependences obtained in this work, namely those of pure iron and the alloys Fe-90% Ni-10%, Fe-60% Ni-40% in the liquid phase are plotted (solid line) in comparison with reference data (non solid line) form different literature sources. Even though the temperature gradient differs, the surface tension decreases with temperature for all investigated materials.

layer of the specimen due to a strong attractive iron-nickel interaction. Otherwise, the element with lower surface tension, in this case nickel, would segregate to the surface in order to minimise the surface free energy [24]. In an attempt to explain the deviation from experimental data to the model, one could presume, that after all, a segregation of nickel did happen and dramatically lowered the surface tension. But, a lot more experimental data have to be collected, to undermine this idea. Additionally, some explanation for the overcoming of the attractive interaction between the unlike atoms would have to be found.

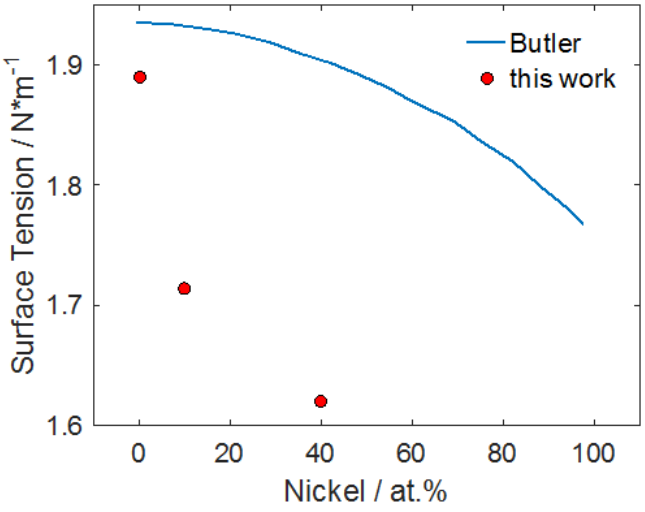

Figure 4.7: Butler model versus measured data: Discrepancies, especially for alloys with an increasing content of nickel, become apparent. Figure adapted from [24].

An other, more promising explanation could be found in the formation of surface oxides. Ozawa et al [25] showed that not only the absolute value of the surface tension, but also the temperature gradient is strongly influenced by the surrounding atmosphere, especially by the partial pressure of oxygen pO_2. Also experiments conducted within the framework of this thesis showed such a dependence. In figure 4.8 the experimental data of Fe-90% Ni-10% can be seen. Two agglomerations can easily be distinguished, a lower one around $\gamma = 1550\,\mathrm{mN{\cdot}m^{-1}}$ and another one at approximately $\gamma = 1700\,\mathrm{mN{\cdot}m^{-1}}$. The higher values occurred, when the experiments were carried out under a reducing, H_2-containing atmosphere. This suggests a strong impact of surface oxides resulting in a completely different surface tension-temperature dependence. Therefore, for a refined surface tension measurement also the influence of the formation of surface oxides should be investigated in more detail. A possible approach of how to tackle this situation is given in section 6.

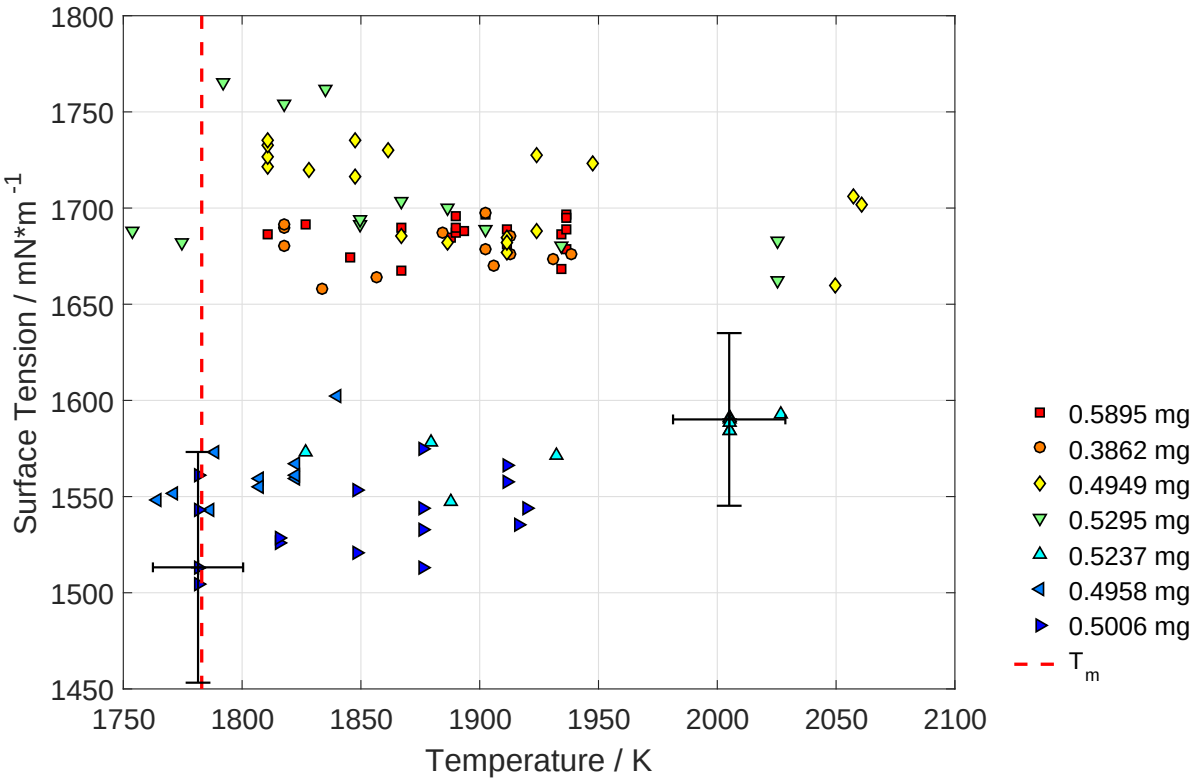

Figure 4.8: Influence of the reducing gas atmosphere on surface tension-temperature dependence of Fe-90% Ni-10%. A different surface tension-temperature behaviour was observed, depending on whether a gas with or without additional hydrogen was used. Experiments conducted under a reducing atmosphere seem to yield higher surface tension values with a larger, negative temperature gradient.

CHAPTER 5

Uncertainty Analysis

The uncertainty budget shown in tabular 5.1 was generated with the software GUM WORKBENCH[30]. The calculations follow the principles given in the DIN/ISO/BIPM Guidelines on the evaluation of uncertainty in measurement and allow an analysis of the contribution of different parameters of the model equation to the uncertainty. A normal distribution of the input quantity was assumed for the surface tension measurements. Leitner [4] has discussed the uncertainty in the temperature measurement conducted via thermal radiation thermometry. Before, the uncertainty was estimated by a constant value of $\Delta T = \pm\ 10\,\mathrm{K}$. He developed a more realistic assessment, yielding temperature-dependent error margins. The mathematical concept and more details on the creation of an uncertaitny budget with GUM can be found in [4]. The uncertainty analysis elaborated in the work of Leitner analogously applies for this work, therefore only an overview will be given in this section. For additional information, please see [4].

The uncertainty budget underlines the importance of an exact peak assignment, as the oscillation frequency values dominate the overall uncertainty.

[30] Version 2.4.1.388, http://www.metrodata.de/ver24.html

Table 5.1: GUM WORKBENCH Uncertainty budget: Input parameters for the calculation of surface tension with equation 2.19
Quantity *QTY*, value of the input parameter *Value*, estimated uncertainty *Std. Uncertainty*, partial derivative of surface tension with respect to the corresponding input value *Sensitivity Coeff.*, product of sensitivity coefficient and standard uncertainty *Uncertainty Contribution*, contribution of the according value to the overall uncertainty in percent *Index*.

Qty	*Value*	*Std. Uncertainty*	*Sensitivity Coeff.*	*Uncertainty Contribution*	*Index*
ν_x	4.1 Hz	0.1 Hz	1.5	0.1 mN·m^{-1}	0.0 %
ν_y	4.2 Hz	0.1 Hz	1.6	0.1 mN·m^{-1}	0.0 %
$\nu_{2,0}$	55.6 Hz	0.5 Hz	14	7.1 mN·m^{-1}	19.8 %
$\nu_{2,-1}$	54.5 Hz	0.5 Hz	14	6.9 mN·m^{-1}	19.0 %
$\nu_{2,+1}$	57.6 Hz	0.5 Hz	15	7.4 mN·m^{-1}	21.3 %
$\nu_{2,-2}$	51.8 Hz	0.5 Hz	13	6.6 mN·m^{-1}	17.2 %
$\nu_{2,+2}$	58.0 Hz	0.5 Hz	15	7.4 mN·m^{-1}	21.5 %
ρ	7096 kg·m^{-3}	25 kg·m^{-3}	$-4.6 \cdot 10^{-3}$	-0.11 mN·m^{-1}	0.0%
m	541.3 mg	0.5 mg	3.5	1.8 mN·m^{-1}	1.2 %

CHAPTER 6

Summary and Outlook

The surface tension as a function of temperature was determined by electromagnetic levitation for three different materials, namely pure iron, Fe-90% Ni-10% and Fe-60% Ni-40%. The resulting data were fitted by the following linear regression model,

$$\gamma(T) = \gamma(T_m) + \frac{d\gamma}{dT}\,(T - T_m)\,, \tag{6.1}$$

yielding the fit parameters $\gamma(T_m)$ and $\frac{d\gamma}{dT}$ summarized in table 6.1.

Table 6.1: Surface tension of the iron-nickel system: Surface tension at the liquidus point $\gamma(T_m)$ and its temperature gradient $\frac{d\gamma}{dT}$ for pure iron and the alloys Fe-90% Ni-10%, Fe-60% Ni-40% in the liquid phase were measured in this work. Further listed are temperature at the melting point T_m, as well as the temperature range of experiments T_{range}.

Material [at%]	T_m [K]	ΔT [K]	$\gamma(T_m)$ [mN·m^{-1}]	$\frac{d\gamma}{dT}$ [mN·m^{-1}K^{-1}]
Fe	1811 [15]	1810 to 2070	1878 ± 84	$-(0.32 \pm 0.04)$
Fe-90% Ni-10%	1783 [19][31]	1755 to 2060	1714 ± 155	$-(0.12 \pm 0.08)$
Fe-60% Ni-40%	1725 [21]	1725 to 1965	1624 ± 171	$-(0.07 \pm 0.06)$

A comparison with values published in literature, the iron data showed a good agreement. Unfortunately no reference data for Fe-90% Ni-10% and Fe-60% Ni-40% was available.

[31] as cited in [20]

In order to analyse the quality of these results, the surface tension predicted by the theoretical Butler model was used. According to this concept, adjusted to the iron-nickel system by Brillo et al [24], higher values should be obtained. Two possible explanations for this discrepancies have been discussed in section 4.5: The Butler model bases on the assumption of prevented aggregation of the component with the lower surface tension, in this case, nickel. In an unlikely event of nickel aggregating to the specimens surface, the surface oscillations could be altered, and calculations would yield a different surface tension.
Another, more realistic cause for this shift would be the generation of surface oxides. The change of the surface tension due to a difference in the used gas atmosphere has been discussed with the help of the Fe-90% Ni-10% data in section 4.3.
Still, the influence of the partial oxygen pressure of the ambient atmosphere on the the surface tension of the sample needs to be investigated appropriately. An implementation of an oxygen detection system is therefore necessary and will be realized as a part of a future research project. This will also improve the reproducibility of the experiments. As surface oxides are suspected to have a great influence on the surface tension, only a comparison between measurements conducted under the same oxygen-reduced atmosphere appears to be valid. With regard to the interests of the steel industry, the installation of an according control in addition to a setup which allows the variation of the oxygen partial pressure would enable a conduction of experiments under conditions similar to the ones of, for example, melting and casting processes. This would ensure a very accurate determination of the surface tension which can then be used as an input parameter for the simulation of such processes.

Appendix

6.1 Material specification

6.1.1 Iron

This 'Certificate of Analysis' was provided by Alfa Aesar[32].

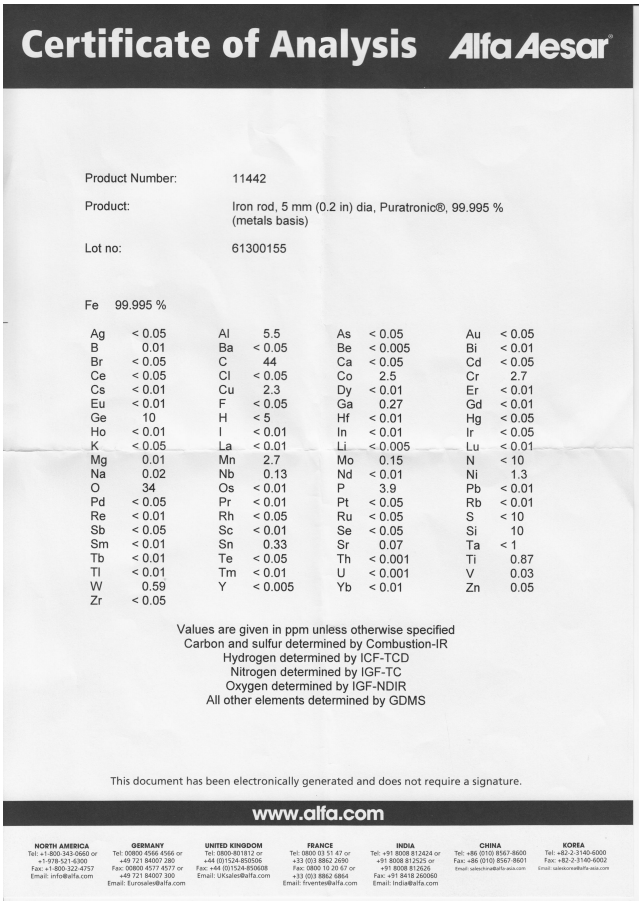

Certificate of Analysis Alfa Aesar

Product Number: 11442

Product: Iron rod, 5 mm (0.2 in) dia, Puratronic®, 99.995 % (metals basis)

Lot no: 61300155

Fe 99.995 %

Ag	< 0.05	Al	5.5	As	< 0.05	Au	< 0.05
B	0.01	Ba	< 0.05	Be	< 0.005	Bi	< 0.01
Br	< 0.05	C	44	Ca	< 0.05	Cd	< 0.05
Ce	< 0.05	Cl	< 0.05	Co	2.5	Cr	2.7
Cs	< 0.01	Cu	2.3	Dy	< 0.01	Er	< 0.01
Eu	< 0.01	F	< 0.05	Ga	0.27	Gd	< 0.01
Ge	10	H	< 5	Hf	< 0.01	Hg	< 0.05
Ho	< 0.01	I	< 0.01	In	< 0.01	Ir	< 0.05
K	< 0.05	La	< 0.01	Li	< 0.005	Lu	< 0.01
Mg	0.01	Mn	2.7	Mo	0.15	N	< 10
Na	0.02	Nb	0.13	Nd	< 0.01	Ni	1.3
O	34	Os	< 0.01	P	3.9	Pb	< 0.01
Pd	< 0.05	Pr	< 0.01	Pt	< 0.05	Rb	< 0.01
Re	< 0.01	Rh	< 0.05	Ru	< 0.05	S	< 10
Sb	< 0.05	Sc	< 0.01	Se	< 0.05	Si	10
Sm	< 0.01	Sn	0.33	Sr	0.07	Ta	< 1
Tb	< 0.01	Te	< 0.05	Th	< 0.001	Ti	0.87
Tl	< 0.01	Tm	< 0.01	U	< 0.001	V	0.03
W	0.59	Y	< 0.005	Yb	< 0.01	Zn	0.05
Zr	< 0.05						

Values are given in ppm unless otherwise specified
Carbon and sulfur determined by Combustion-IR
Hydrogen determined by ICF-TCD
Nitrogen determined by IGF-TC
Oxygen determined by IGF-NDIR
All other elements determined by GDMS

This document has been electronically generated and does not require a signature.

www.alfa.com

NORTH AMERICA Tel: +1-800-343-0660 or +1-978-521-6300 Fax: +1-800-322-4757 Email: info@alfa.com
GERMANY Tel: 00800 4566 4566 or +49 721 84007 280 Fax: 00800 4577 4577 or +49 721 84007 300 Email: Eurosales@alfa.com
UNITED KINGDOM Tel: 0800-801812 or +44 (0)1524-850506 Fax: +44 (0)1524-850608 Email: UKsales@alfa.com
FRANCE Tel: 0800 03 51 47 or +33 (0)3 8862 2690 Fax: 0800 10 20 67 or +33 (0)3 8862 6864 Email: frventes@alfa.com
INDIA Tel: +91 8008 812424 or +91 8008 812525 or +91 8008 812626 Fax: +91 8418 260060 Email: India@alfa.com
CHINA Tel: +86 (010) 8567-8600 Fax: +86 (010) 8567-8601 Email: saleschina@alfa-asia.com
KOREA Tel: +82-2-3140-6000 Fax: +82-2-3140-6002 Email: salesKorea@alfa-asia.com

[32] Alfa Aesar, Thermo Fisher (Kandel) GmbH, Karlsruhe, Germany

6.1.2 Iron-nickel alloy: Fe-90% Ni-10%

Two different Fe-90% Ni-10% batches from the same casting were used. Their chemical compositions are illustrated below. In order to verify the analysis of 'PROBE E', a new analysis was conducted with energy dispersive X-ray spectroscopy.

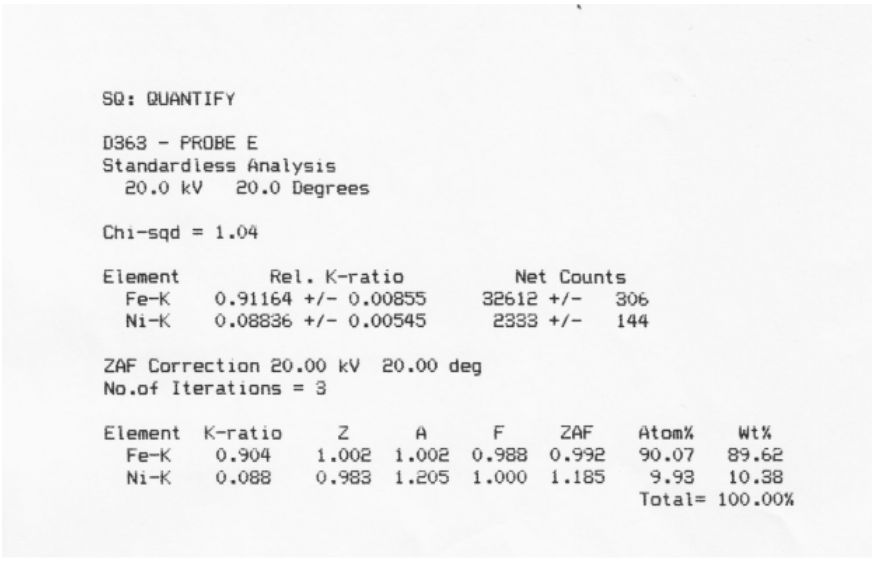

```
SQ: QUANTIFY

D363 - PROBE E
Standardless Analysis
  20.0 kV   20.0 Degrees

Chi-sqd = 1.04

Element        Rel. K-ratio          Net Counts
  Fe-K    0.91164 +/- 0.00855     32612 +/-   306
  Ni-K    0.08836 +/- 0.00545      2333 +/-   144

ZAF Correction 20.00 kV  20.00 deg
No.of Iterations = 3

Element  K-ratio     Z      A      F     ZAF    Atom%    Wt%
  Fe-K    0.904    1.002  1.002  0.988  0.992   90.07   89.62
  Ni-K    0.088    0.983  1.205  1.000  1.185    9.93   10.38
                                                Total= 100.00%
```

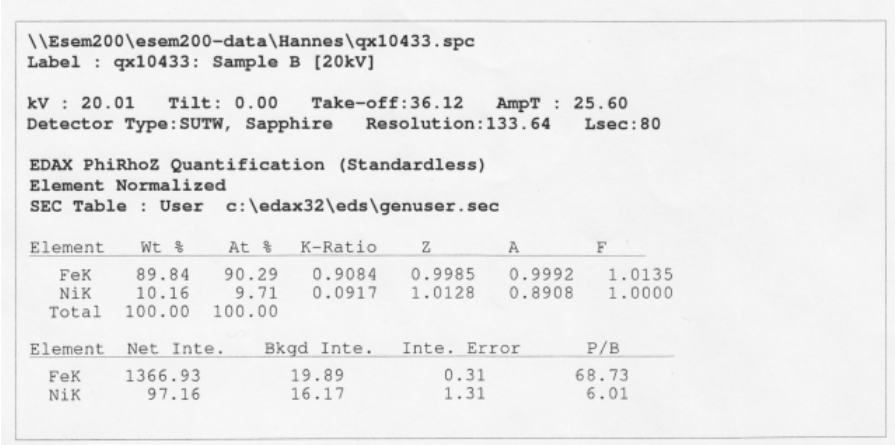

```
\\Esem200\esem200-data\Hannes\qx10433.spc
Label : qx10433: Sample B [20kV]

kV : 20.01   Tilt: 0.00   Take-off:36.12   AmpT : 25.60
Detector Type:SUTW, Sapphire   Resolution:133.64   Lsec:80

EDAX PhiRhoZ Quantification (Standardless)
Element Normalized
SEC Table : User  c:\edax32\eds\genuser.sec

Element    Wt %     At %   K-Ratio    Z        A        F
   FeK     89.84    90.29    0.9084   0.9985   0.9992   1.0135
   NiK     10.16     9.71    0.0917   1.0128   0.8908   1.0000
 Total    100.00   100.00

Element  Net Inte.    Bkgd Inte.   Inte. Error      P/B
  FeK     1366.93         19.89          0.31        68.73
  NiK       97.16         16.17          1.31         6.01
```

6.1.3 Iron-nickel alloy: Fe-60% Ni-40%

The analysis of Fe-60% Ni-40% was done by our project partner Böhler[33].

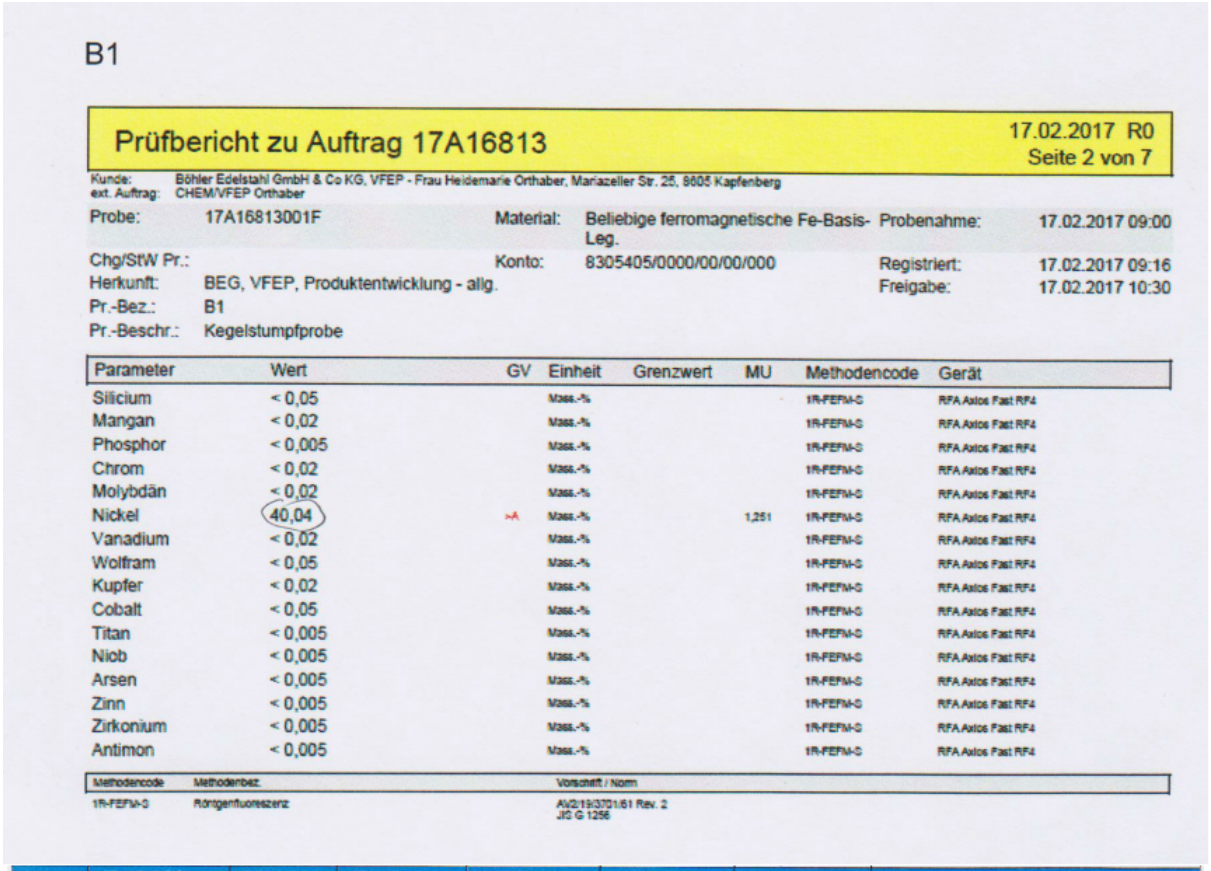

B1

Prüfbericht zu Auftrag 17A16813 17.02.2017 R0 Seite 2 von 7

Kunde: Böhler Edelstahl GmbH & Co KG, VFEP - Frau Heidemarie Orthaber, Mariazeller Str. 25, 8605 Kapfenberg
ext. Auftrag: CHEM/VFEP Orthaber

Probe:	17A16813001F	Material:	Beliebige ferromagnetische Fe-Basis-Leg.	Probenahme:	17.02.2017 09:00
Chg/StW Pr.:		Konto:	8305405/0000/00/00/000	Registriert:	17.02.2017 09:16
Herkunft:	BEG, VFEP, Produktentwicklung - allg.			Freigabe:	17.02.2017 10:30
Pr.-Bez.:	B1				
Pr.-Beschr.:	Kegelstumpfprobe				

Parameter	Wert	GV	Einheit	Grenzwert	MU	Methodencode	Gerät
Silicium	< 0,05		Mass.-%			1R-FEFM-S	RFA Axios Fast RF4
Mangan	< 0,02		Mass.-%			1R-FEFM-S	RFA Axios Fast RF4
Phosphor	< 0,005		Mass.-%			1R-FEFM-S	RFA Axios Fast RF4
Chrom	< 0,02		Mass.-%			1R-FEFM-S	RFA Axios Fast RF4
Molybdän	< 0,02		Mass.-%			1R-FEFM-S	RFA Axios Fast RF4
Nickel	40,04	>A	Mass.-%		1,251	1R-FEFM-S	RFA Axios Fast RF4
Vanadium	< 0,02		Mass.-%			1R-FEFM-S	RFA Axios Fast RF4
Wolfram	< 0,05		Mass.-%			1R-FEFM-S	RFA Axios Fast RF4
Kupfer	< 0,02		Mass.-%			1R-FEFM-S	RFA Axios Fast RF4
Cobalt	< 0,05		Mass.-%			1R-FEFM-S	RFA Axios Fast RF4
Titan	< 0,005		Mass.-%			1R-FEFM-S	RFA Axios Fast RF4
Niob	< 0,005		Mass.-%			1R-FEFM-S	RFA Axios Fast RF4
Arsen	< 0,005		Mass.-%			1R-FEFM-S	RFA Axios Fast RF4
Zinn	< 0,005		Mass.-%			1R-FEFM-S	RFA Axios Fast RF4
Zirkonium	< 0,005		Mass.-%			1R-FEFM-S	RFA Axios Fast RF4
Antimon	< 0,005		Mass.-%			1R-FEFM-S	RFA Axios Fast RF4

Methodencode	Methodenbez.	Vorschrift / Norm
1R-FEFM-S	Röntgenfluoreszenz	AV2/19/3701/61 Rev. 2 JIS G 1256

	Fe60% [g]	Ni40% [g]	Fe-Ist %	Ni-Ist %	~Spuren %	Σ Fe_Ni Analyse	
B1	210	140	59,625	40,04	0,335	99,665	Ohne Lunker

[33] Böhler Edelstahl, Kapfenberg, Austria

Abbrevations

EML	electromagnetic levitation
TU Graz	Graz University of Technology
FFT	Fast Fourier Transform

Bibliography

[1] I. Egry, G. Lohöfer, and S. Sauerland. Measurements of thermophysical properties of liquid metals by noncontact techniques. *International Journal of Thermophysics*, 14(3):573–584, May 1993. doi:10.1007/BF00566054.

[2] K. Aziz. *Surface Tension Measurements of Liquid Metals and Alloys by Oscillating Drop Technique in combination with an Electromagnetic Levitation Device.* PhD thesis, Graz University of Technology, 2016. URL: https://www.tugraz.at/fileadmin/user_upload/Institute/IEP/Thermophysics_Group/Files/Diss-AzizKirmanj.pdf.

[3] A. Schmon. *Density Determination of Liquid Metals by Means of Containerless Techniques.* PhD thesis, Graz University of Technology, 2016. URL: https://www.tugraz.at/fileadmin/user_upload/Institute/IEP/Thermophysics_Group/Files/Diss-SchmonAlexander.pdf.

[4] T. Leitner. Thermophysical properties of liquid aluminium determined by means of electromagnetic levitation. Master's thesis, 2016.

[5] D. Herlach, R. Cochrane, I. Egry, H. Fecht, and A. Geer. Containerless processing in the study of metallic melts and their solidification. *International Materials Reviews*, 38(6):273–347, 1993. doi:10.1179/095066093790326267.

[6] J. Brillo, G. Lohöfer, F. Schmidt-Hohagen, and S. Schneider. Thermophysical property measurements of liquid metals by electromagnetic levitation. *International Journal of Materials and Product Technology*, 26(3):247–273, 2006. doi:10.1504/ijmpt.2006.009469.

[7] D. L. Cummings and D. A. Blackburn. Oscillations of magnetically levitated aspherical droplets. *Journal of Fluid Mechanics*, 224(1):395, March 1991. URL: http://journals.cambridge.org/abstract_S0022112091001817, doi:10.1017/s0022112091001817.

[8] L. Rayleigh. On the capillary phenomena of jets. *Proceedings of the Royal Society of London*, 29(196-199):71–97, January 1879. doi:10.1098/rspl.1879.0015.

[9] E. C. Okress, D. M. Wroughton, G. Comenetz, P. H. Brace, and J. C. R. Kelly. Electromagnetic levitation of solid and molten metals. *Journal of Applied Physics*, 23(5):545–552, 1952. doi:10.1063/1.1702166.

[10] F. H. Busse. Oscillations of a rotating liquid drop. *Journal of Fluid Mechanics*, 142(-1):1, May 1984. URL: http://journals.cambridge.org/abstract_S0022112084000963, doi:10.1017/s0022112084000963.

[11] K. Aziz, A. Schmon, E. Kaschnitz, J. Rattenberger, and G. Pottlacher. Measurement of surface tension of Cu-5Sn by an oscillating drop technique. *International Journal of Thermophysics*, 37(2):0, January 2016. URL: http://dx.doi.org/10.1007/s10765-015-2023-z, doi:10.1007/s10765-015-2023-z.

[12] F. Henning. *Temperaturmessung*. Springer Science Business Media, 1977. doi:10.1007/978-3-642-81138-8.

[13] D. R. Lide. *CRC Handbook of Chemistry and Physics, 84th Edition*. Taylor & Francis, 2003. URL: https://www.crcpress.com/CRC-Handbook-of-Chemistry-and-Physics-84th-Edition/Lide/p/book/9780849304842.

[14] Leitner T, O. Klemmer, M. Leitner, and G. Pottlacher. Untersuchung der temperaturabhängigen Oberflächenspannung des Eisen-Nickel Systems mittels elektromagnetischer Levitation. In *Temperatur 2017*, page 273, 2017.

[15] Landolt-Börnstein. Thermodynamic properties of elements, callcium to germanium. In *Pure Substances. Part 1: Elements and Compounds from AgBr to Ba3N2*, pages 25–50. Springer Nature, 1999. doi:10.1007/10652891_5.

[16] J. Brillo and I. Egry. Surface tension of nickel, copper, iron and their binary alloys. *Journal of Materials Science*, 40(9-10):2213–2216, May 2005. URL: http://link.springer.com/article/10.1007/s10853-005-1935-6, doi:10.1007/s10853-005-1935-6.

[17] K. Aziz, A. Schmon, and G. Pottlacher. Measurement of surface tension of liquid nickel by the oscillating drop technique. *High Temperatures-High Pressures*, pages 475–481, 2015.

[18] R. Brooks, I. Egry, S. Seetharaman, and D. Grant. Reliable data for high-temperature viscosity and surface tension: results from a european project. *High Temperatures-High Pressures*, 33(6):631–637, 2001. doi:10.1068/htwu323.

[19] T. Kase. On the equilibrium diagram of the iron-carbon-nickel system. *Sience Reorts of the Tohoklu Imperial University*, 1:174–217, 1925.

[20] L. Swartzendruber, V. Itkin, and C. Alcock. The Fe-Ni (iron-nickel) system. *Journal of phase equilibria*, 12(3):288–312, 1991. URL: https://link.springer.com/article/10.1007%2FBF02649918, doi:10.1007/BF02649918.

[21] J. Brillo and I. Egry. Density and excess volume of liquid copper, nickel, iron, and their binary alloys. *Zeitschrift für Metallkunde*, 95(8):691–697, August 2004. doi:10.3139/146.018009.

[22] R. Brooks and K. Mills. Measurement of the thermophysical properties of melts by a levitated-drop method. *High Temperatures. High Pressures*, 25(6):657–664, 1993.

[23] J.A.V. Butler. The thermodynamics of the surfaces of solutions. *Proceedings of the Royal Society of London. Series A*, 135(827):348–375, 1932. URL: http://rspa.royalsocietypublishing.org/content/135/827/348.full.pdf, doi:10.1098/rspa.1932.0040.

[24] J. Brillo, D. Chatain, and I. Egry. Surface tension of liquid binary alloys–theory versus experiment. *International Journal of Materials Research*, 100(1):53–58, 2009. URL: http://www.hanser-elibrary.com/doi/abs/10.3139/146.101787, doi:10.3139/146.101787.

[25] S. Ozawa, S. Takahashi, H. Fukuyama, and M. Watanabe. Temperature dependence of surface tension of molten iron under reducing gas atmosphere. *Journal of Physics: Conference Series*, 327:012020, December 2011. doi:10.1088/1742-6596/327/1/012020.

List of Figures

List of Tables